ADVANCED REVIEW: Diffusion Monte Carlo Approaches for Studying Nuclear Quantum Effects in Fluxional Molecules

Ryan J. DiRisio[1], Jacob M. Finney[1], and Anne B. McCoy*[1]

[1]Department of Chemistry, University of Washington, Seattle, WA 98195 USA

Abstract

Diffusion quantum Monte Carlo (DMC) provides a powerful approach for obtaining the ground state energy and wave function of molecules, ions and molecular clusters. The approach is uniquely well-suited for studies of fluxional molecules, which undergo large amplitude vibrational motions even in their ground state. In contrast to the electronic structure problem, where the wave function must be antisymmetric with respect to exchange of any pair of electrons, the wave function for the ground vibrational state is nodeless. This greatly simplifies the application of DMC for vibrational problems. Because there is not a single potential function that can be used to describe the intra- and intermolecular interactions in all molecular systems, most methods that are used to describe nuclear quantum effects rely on a carefully chosen zero-order description of the molecular vibrations. In contrast, DMC calculations can be performed in Cartesian coordinates, making the DMC algorithm easily transferable between different chemical systems. In this contribution, the theory that underlies DMC will be discussed along with important considerations for performing DMC calculations. Extensions for evaluating vibrationally excited states and molecular properties are also discussed. Insights that can be obtained from DMC calculations are illustrated in the context of the protonated water clusters.

*Corresponding author; email:abmccoy@uw.edu

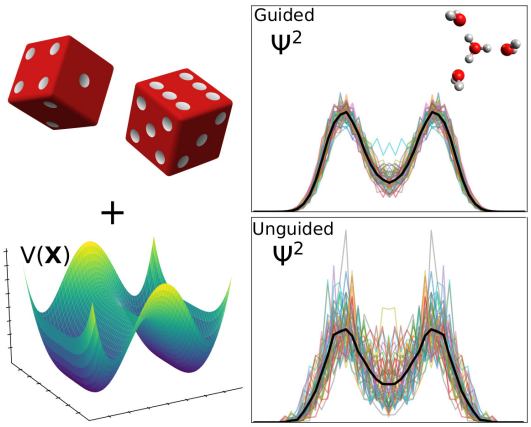

GRAPHICAL ABSTRACT: Diffusion Monte Carlo provides a powerful tool for studying the vibrational landscape of systems that display large amplitude motions. With the introduction of guiding functions, this approach can be used to obtain high quality vibrational wave functions that enhance our understanding of these molecules, ions and clusters.

1 Introduction

In 1929, Dirac stated that [1]

> The underlying physical laws necessary for the mathematical theory of a large part of physics and the whole of chemistry are thus completely known, and the difficulty is only that the exact application of these laws leads to equations much too complicated to be soluble. It therefore becomes desirable that approximate practical methods of applying quantum mechanics should be developed, which can lead to an explanation of the main features of complex atomic systems without too much computation.

While Dirac made this statement long before modern computers were invented and in the context of the development of the Dirac equation, the general sentiment applies to many areas of molecular quantum mechanics.

Of the currently available methods for solving quantum mechanical problems in chemistry, some of the most promising avenues for meeting Dirac's challenge are those that are based on diffusion quantum Monte Carlo (DMC). One particularly attractive feature of DMC is that it is amenable to high levels of parallelization, and for many years the electronic structure theory community has looked to DMC as a promising approach for developing and implementing algorithms on the the state of the art large-scale supercomputing resources.[2, 3] While there has been much activity in developing and extending approaches for obtaining accurate solutions to the electronic Schrödinger equation using quantum Monte Carlo approaches, and the reader is referred to reviews of that work,[4, 5, 6, 7, 8, 9, 10, 11] these approaches can also provide powerful tools for exploring the solution to the nuclear Schrödinger equation. The present contribution provides a discussion of DMC in the context of vibrational problems.

There are several important differences between the vibrational and electronic structure problems. The first and perhaps most significant comes from the potential surface. All of the interactions in the electronic Hamiltonian are Coulombic and the general form of the potential is the same if one considers the hydrogen molecule or a protein. In contrast, the vibrational Schrödinger equation is based on a potential surface, which is a function of the $3N-6$ vibrational coordinates. While the values of these potential energies can be obtained by solving the electronic Schödinger equation through the Born-Oppenheimer approximation, there is no generic form for the potential energy that can describe any system of interest. Further, the choice of vibrational coordinates depends on the bonding of the system and the energy range one is interested in considering. This makes it difficult to develop a general approach that can be equally valid for any molecular system that one has a potential surface for. One could argue that vibrational perturbation theory,[12, 13] or methods based on harmonic treatments of molecular vibrations [14] display this generality, but both will break down in the case of large amplitude vibrations. Other basis-set [15] or multi-configurational Hartree [16] approaches can capture these large amplitude motions, but they are limited to small or moderate sized molecular systems and the approach and coordinates require adjustment based on the bonding in the system of interest. In this way, DMC, which is typically implemented in Cartesian coordinates, holds a large advantage. We have recently developed a general implementation of DMC for vibrational systems called PyVibDMC, which exploits the generality of the approach.[17]

A second key difference between the vibrational and electronic structure problems is found in the nature of the ground state wave function. Since electrons are Fermions, the electronic wave function must be anitsymmetric with respect to exchange of any pair of electrons. In contrast,

the ground state solution to the vibrational Schrödinger equation is nodeless. This greatly simplifies the DMC algorithm for the nuclear problem compared to the electronic structure one. On the other hand, the spacing among the vibrational levels is generally much smaller than the spacings among the electronic states, and often we wish to explore both the ground and excited states. This introduces challenges for DMC for vibrational problems that are often not considered from the electronic structure standpoint.

In the discussion that follows, we will review the DMC algorithm with an eye toward its application to vibrational problems and more specifically vibrations in molecules that undergo large amplitude vibrational motions even in their ground states, e.g. fluxional molecules. We will discuss choices for guiding functions and how the choice of such functions affects the convergence of the simulation. We will also discuss methods that can be used to evaluate properties (e.g. expectation values and excited state information) from the DMC wave function. The discussion will be placed in the context of studies of hydrogen bonding and proton delocalization in protonated water cluster systems. These systems have been studied extensively over the past twenty years,[18, 19, 20, 21, 22, 23, 24, 25, 26, 27, 28, 29] and spectroscopic studies of the three smallest clusters in which the hydronium ion is solvated by one to three water molecules show a large variability in the OH stretch frequency of the OH vibrations involved in hydrogen bonds between the hydronium core and a flanking water molecule. All calculations presented in this review were performed using PyVibDMC.[1] [30]

2 Overview of Diffusion Monte Carlo

2.1 General theory

The diffusion Monte Carlo (DMC) approach is based on solving the time-dependent Schrödinger equation, which has been rotated to imaginary time by replacing the time variable, t, with $\tau = it/\hbar$. Expressed in this way,[31, 32]

$$\frac{d\Psi}{d\tau} = -(\hat{H} - E_{\text{ref}}))\Psi(\mathbf{x}, \tau) \tag{1}$$

where for a molecule that contains N atoms,

$$\hat{H} = \sum_{k=1}^{N} \frac{\hat{\mathbf{p}}_k^2}{2m_k} + V(\mathbf{x}) \tag{2}$$

The general solution to Eq. 1 can be expressed as

$$\Psi(\mathbf{x}, \tau) = \sum_n c_n(\tau = 0) e^{-(E_n - E_{\text{ref}})\tau} \varphi_n(\mathbf{x}) \tag{3}$$

where

$$\hat{H}\varphi_n(\mathbf{x}) = E_n \varphi_n(\mathbf{x}) \tag{4}$$

In the limit of large τ,

$$\Psi(\mathbf{x}, \tau) = c_0(\tau = 0) e^{-(E_0 - E_{\text{ref}})\tau} \varphi_0(\mathbf{x}) \tag{5}$$

[1] The PyVibDMC package is available for download and installation on GitHub and the Python Package Index (PyPI).[30]

In the above expressions, the energy has been shifted by a value, $E_{\rm ref}$. This parameter will be used in the simulation to obtain an estimate to E_0 by requiring that the amplitude of Ψ remains constant throughout the simulation.

The above expressions are general and do not require Monte Carlo approaches to solve nor do they appear to be related to diffusion. The diffusion aspect of DMC arises from the isomorphism between Eq. 1 and a diffusion equation with a coordinate-dependent rate process.[31, 32] This provides one approach for obtaining the working equations for DMC. Here we will utilize the solution to the time-dependent Schrödinger equation based on using a Trotter-Suzuki expansio of the propagators [33, 34, 35, 36, 37]

$$\begin{aligned} \Psi(\mathbf{x}, \tau + \Delta\tau) &= e^{-(\hat{H} - E_{\rm ref})\Delta\tau} \Psi(\mathbf{x}, \tau) \\ &\approx e^{-(\hat{V} - E_{\rm ref})\Delta\tau} e^{-\hat{T}\Delta\tau} \Psi(\mathbf{x}, \tau) \end{aligned} \tag{6}$$

and express

$$\Psi(\mathbf{x}, \tau) = \frac{f(\mathbf{x}, \tau)}{\Phi_{\rm T}(\mathbf{x})} \tag{7}$$

where $f(\mathbf{x}, \tau)$ is represented by a weighted sum of localized functions, $g(\mathbf{x})$,

$$f(\mathbf{x}, \tau) = \sum_j w_j(\tau) g_j(\mathbf{x} - \mathbf{x}_j(\tau)) \tag{8}$$

and $\Phi_{\rm T}$ provides a trial wave function, referred to as a guiding function in the following discussion, which provides a good approximation to the ground state wave function for the system of interest. Considerations in choosing $\Phi_{\rm T}$ will be discussed in the following section. In the discussion that follows these localized functions will be referred to as walkers.

Substituting Ψ in Eq. 7 into Eq. 1, we obtain the working equations,[38]

$$\begin{aligned} \frac{df}{d\tau} &= \sum_{k=1}^{N} \left[\frac{\hbar^2}{2m_k} \nabla_k^2 - \vec{\nabla}_k \cdot \vec{D}_k(\mathbf{x}) \right] f(\mathbf{x}) \\ &\quad - \left(E_{\rm L}(\mathbf{x}) - E_{\rm ref} \right) f(\mathbf{x}) \end{aligned} \tag{9}$$

where

$$E_{\rm L} = \frac{\hat{H}\Phi_{\rm T}}{\Phi_{\rm T}} \tag{10}$$

is the local energy and

$$\vec{D}_k(\mathbf{x}) = \frac{\hbar^2}{m_k} \frac{1}{\Phi_{\rm T}(\mathbf{x})} \vec{\nabla}_k \Phi_{\rm T}(\mathbf{x}) \tag{11}$$

is the drift term. Analyzing the action of the propagator based on Eq. 9 on a single localized function, we find that the first term leads to the displacement of the center of the function by $\mathbf{D}\Delta\tau$ and an increase of the width of the localized function in the Cartesian coordinates of the kth atom to

$$\sigma_k = \hbar\sqrt{\Delta\tau / m_k} \tag{12}$$

To retain the form of f as a sum of localized functions, rather than allowing the widths of each of the $g(\mathbf{x} - \mathbf{x}_j)$ functions to increase at each time step, the position of the center of each of these functions is further displaced by an amount, which is represented by δ_j. The values of the

elements of δ_j are selected from a Gauss-random distribution, with a width in the coordinates of the kth atom that is given by σ_k. In this way, the position of the jth walker is moved from $\mathbf{x}_j(\tau)$ to $\mathbf{x}'_j(\tau)$, where

$$\mathbf{x}'_j(\tau) = \mathbf{x}_j(\tau) + \mathbf{D}(\mathbf{x}_j)\Delta\tau + \delta_j \tag{13}$$

Before considering the final term in Eq. 9, we consider whether this displacement satisfies microscopic reversibility, by comparing the probability of moving from $\mathbf{x}'_j(\tau)$ to $\mathbf{x}_j(\tau)$, where

$$\mathbf{x}_j(\tau) = \mathbf{x}'_j(\tau) + \mathbf{D}_j(\mathbf{x}'_j)\Delta\tau + \delta'_j \tag{14}$$

to the probability of the displacement from $\mathbf{x}_j(\tau)$ to $\mathbf{x}'_j(\tau)$. Since, in general, $\mathbf{D}_j(\mathbf{x}'_j) \neq -\mathbf{D}_j(\mathbf{x}_j)$, δ'_j will not be the same as $-\delta_j$.

The probability of making a move from $\mathbf{x}'_j$ to $\mathbf{x}_j$, $P\left(\mathbf{x}'_j \rightarrow \mathbf{x}_j\right)$ has two contributions. The first is the probability amplitude at $\mathbf{x}'_j$, which is approximated by $\Phi_{\mathrm{T}}^2(\mathbf{x}'_j)$. The second is the value of the Gaussian function that was sampled to obtain the δ'_j. As such, whether or not a move is accepted is determined by whether the move from x' to x is as or more probable than the move from x to x'. This relative probability is approximated by

$$\mathcal{P}_j = \frac{P\left(\mathbf{x}'_j \rightarrow \mathbf{x}_j\right)}{P\left(\mathbf{x}_j \rightarrow \mathbf{x}'_j\right)} = \frac{\Phi_{\mathrm{T}}^2(\mathbf{x}'_j)}{\Phi_{\mathrm{T}}^2(\mathbf{x}_j)} \prod_{k=1}^{N} \exp\left[-\left(\left|\delta'_{k,j}\right|^2 - \left|\delta_{k,j}\right|^2\right)/2\sigma_k^2\right] \tag{15}$$

If $\mathcal{P}_j$ is larger than a random number taken from a uniform random distribution on the range of [0,1], the move is accepted, and $\mathbf{x}_j(\tau + \Delta\tau) = \mathbf{x}'_j$. Otherwise, the move is rejected, and $\mathbf{x}_j(\tau + \Delta\tau) = \mathbf{x}_j(\tau)$. In this way, displacements for which $P\left(\mathbf{x}'_j \rightarrow \mathbf{x}_j\right) > P\left(\mathbf{x}_j \rightarrow \mathbf{x}'_j\right)$ will always be accepted otherwise the value of $\mathcal{P}_j$ provides the probability that the move will be accepted. Operationally, we aim for the fraction of the moves that are rejected to be no larger than 0.2% of the ensemble size. This acceptance/rejection algorithm is referred to as the Metropolis step.

The final term in Eq. 9 takes the role of the potential energy in Eq. 1. Since f is represented as an ensemble of localized functions we find that the effect of this term is to update the value of w_j in Eq. 8 based on the value of

$$P_j(\tau) = \exp\left[-(E_{\mathrm{L}}(\mathbf{x}_j(\tau + \Delta\tau)) - E_{\mathrm{ref}}(\tau))\Delta\tau\right] \tag{16}$$

Updating the w_j can be accomplished through one of two approaches.

The first, termed continuous weighting, allows the weights of the walkers to be updated at each time step based on [39]

$$w_j(\tau + \Delta\tau) = P_j(\tau)w_j(\tau) \tag{17}$$

This approach can be effective for short time propagations, but at longer times some of the w_j become very large while others approach zero. This results in the ensemble containing a large number of walkers that have very small weights and a small number of walkers that carry most of the weight. To avoid this problem, we limit the range of allowed values for the w_j by defining $w_{\max}$ and $w_{\min}$, which provide the maximum and minimum allowed values for the w_j. For each of the walkers that has a weight that is smaller than $w_{\min}$, the following steps are followed:

1. The walker in the ensemble that has the largest weight is identified.

2. The coordinates of the low-weight walker are replaced by those of the walker with the largest weight.

3. The weights of the low- and largest-weight walkers are replaced by half the value of the weight of the largest weight walker.

Likewise, if after this procedure the weights of one or more of the walkers exceed $w_{\max}$ an analogous procedure is followed. This removal of walkers is referred to as branching. We have found that using $0.01 < w_{\min} < 0.1$ and $w_{\max} = 20$ results in a stable simulation.[40]

An alternative to continuous weighting is discrete weighting.[41] In this approach, the weights of all of the walkers are set to 1. While in continuous weighting, the number of walkers remains constant throughout the simulation, in discrete weighting the ensemble size fluctuates. In discrete weighting, we once again start by evaluating $P_j(\tau)$ using Eq. 16. The integer part of $P_j(\tau)$ provides the number of walkers centered at $\mathbf{x}_j$ that will be in the ensemble at the start of the next step in the propagation. The fractional part of $P_j(\tau)$ provides the probability that one additional walker will be introduced at these coordinates. The determination of whether (or not) to introduce this additional walkers is made by comparing the fractional part of $P_j(\tau)$ to a random number taken from a uniform random distribution on the range of [0,1]. If the random number is smaller than the fractional part of $P_j(\tau)$, an additional walker that is centered at $\mathbf{x}_j$ is added to the ensemble. As noted above, in the discrete weighting scheme, all of the weights are constrained to be equal to one.

Once the weights have been determined, the final step of the simulation is to evaluate E_{ref}. As noted above, the purpose of E_{ref} is to ensure that the amplitude of the wave function remains constant. This is achieved by keeping the sum of the weights constant. To this end,[32]

$$E_{\text{ref}}(\tau) = \frac{\sum_j w_j(\tau) E_{\text{L}}(\mathbf{x_j}(\tau))}{\sum_j w_j(\tau)} - \frac{\alpha \sum_j w_j(\tau)}{\sum_j w_j(\tau = 0)} \tag{18}$$

where α is a simulation parameter, which is introduced to keep the ensemble size constant. We have found that using $\alpha = 0.5/\Delta\tau$ works well.[42, 43] This is illustrated in Figures 6 and S2 of Ref. [43]. One can see that we achieve the desired effect as in cases where the sum of the weights becomes smaller than the sum of the weights at $\tau = 0$, E_{ref} is increased, placing more walkers in the classically allowed region of configuration space where $\exp[-(E_{\text{L}} - E_{\text{ref}})] > 1$, thereby leading to an increase in the sum of the weights at the next time step.

The above procedure, which can be summarized as

1. Evaluate the drift term, $\mathbf{D}$ at the current coordinates of the walker.
2. Generate displacements of the walkers, δ.
3. Evaluate $\mathbf{x}'$ using Eq. 13.
4. Evaluate $\mathcal{P}$ using Eq. 15 and determine if the move is accepted or rejected. Based on this, evaluate $\mathbf{x}(\tau + \Delta\tau)$.
5. Evaluate $E_{\text{L}}(\mathbf{x}(\tau + \Delta\tau))$ using Eq. 10.
6. Evaluate $P(\tau)$ using Eq. 16.
7. Update the weights, w, and branch walkers as needed.
8. Update E_{ref}.

is repeated for sufficient time steps to obtain converged results. For time steps of 1.0 a.u., generally runs of 10 000 or more time steps are required.

The above description is based on performing the DMC simulation in Cartesian coordinates as this is the most common choice. One can use other coordinates with minor adjustments to the above algorithm to account for the coupling terms in the kinetic energy operator.[44] Likewise, Buch [45] and Benoit and Clary [46] have developed approaches for performing DMC simulations of molecular clusters composed of rigid molecules.

2.2 Initializing the ensemble of walkers

The above procedure is predicated on an initial distribution of walkers. Over the years, we have employed several approaches to obtain an initial distribution of walkers. One option is to localize all of the walkers in a local minimum in the potential.[47] This approach can be advantageous if the potential contains multiple minima and the state of interest is not localized in the global minimum. In most cases, though, such a bias is not desired. Another simple algorithm involves placing the center of mass of the system of interest at the origin, and multiplying the Cartesian coordinates of all of the atoms by a scaling factor. This places the walkers in a high energy region of the potential, from which the ensemble of walkers can relax toward the potential minimum. A third approach samples the coordinates based on the harmonic ground state probability amplitude obtained through a normal mode analysis of the potential.[48] For vibrations that are highly anharmonic, the width of the distribution in these coordinates may be expanded by multiplying the sampled normal mode coordinate by a constant scaling factor. Finally, when the ground state wave function is expected to sample multiple minima, the initial ensemble may be generated by sampling geometries from each of the relevant minima. This final approach should be employed when one is studying partially deuterated systems where the energy differences among the isotopologues are small.

2.3 Potential energy functions

A central ingredient in the Hamiltonian in Eq. 2 is the potential function, $V(\mathbf{x})$. While for electronic structure calculations, the potential can be expressed as the sum of Coulombic terms, for vibrational problems we typically average the full Hamiltonian over the electronic wave function for the state of interest. This is accomplished through the Born-Oppenheimer approximation, and the resulting potential energy as a function of the nuclear coordinates becomes the potential energy function found in Eq. 2. As the ultimate goal of this work is to make comparisons with spectra, potential energies with accuracies that are comparable to those obtained from CCSD(T) calculations are desired. The expense of CCSD(T) calculations even for the smallest molecules coupled to the large ensemble sizes needed for DMC simulations, make direct calculation of the electronic energies intractable. Rather, we rely on potential surfaces that have been fit by others, and much of our work has relied on potential functions that were fit to permutationally invariant polynomials by Bowman and co-workers.[49] For example, they have fit potentials for protonated water clusters,[50, 51] CH_5^+,[52] H_5^+[53] as well as water clusters,[54, 55, 56] and all of these potentials have been used for DMC studies. Other recent studies have employed the MB-pol potentials developed by the Paesani group.[57, 58, 59, 60] While these potential functions provide highly accurate descriptions of the molecular system of interest, they are not exact fits to the underlying electronic structure data. Additionally, the underlying electronic structure calculations, while highly accurate, are not exact solutions to the electronic Schrödinger equa-

tion. For this reason, we choose to focus on using 1 a.u. time steps for our DMC calculations as these have been found to be sufficiently small time step to obtain an accuracy of on the order of 5-10 cm^{-1}. This level of accuracy typically exceeds that of the potential surface that is used for the calculations. The reliance on potential surfaces is a current limitation of the DMC approach, and we are actively exploring opportunities to develop potentials for DMC calculations *on-the-fly*.[47]

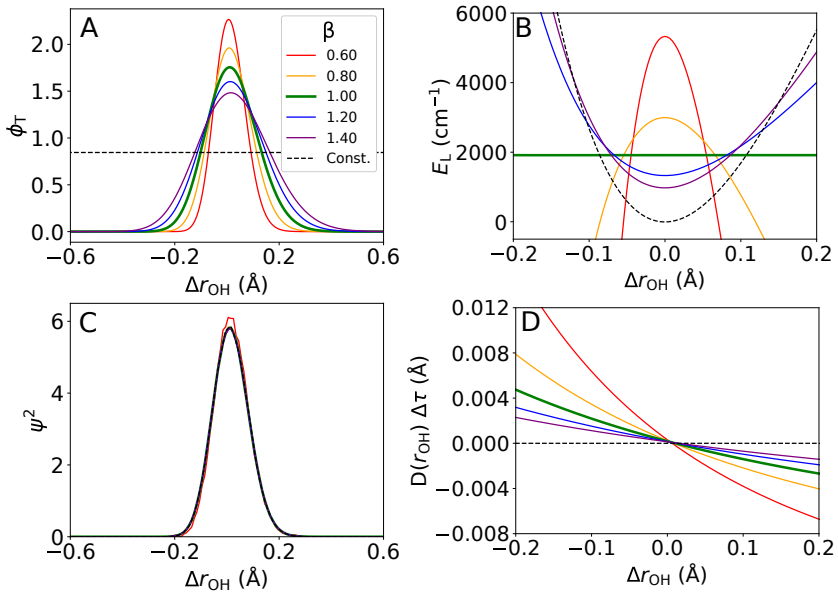

Figure 1: (A) The ϕ_{T} plotted as a function of the displacements of one of the OH bond lengths from their equilibrium values, $\Delta r_{\mathrm{OH}} = r_{\mathrm{OH}} - r_{\mathrm{OH,e}}$, where $r_{\mathrm{OH,e}} = 0.9598$ Å, and the OH stretch wave function that is obtained by solving the one-dimensional Schrödinger equation is plotted in green. The red, orange, blue and purple curves provide the wave function after broadening this function by 0.6, 0.8, 1.2 and 1.4, respectively. The black dashed line represents the constant guiding function used in an unguided DMC calculation. (B) The local energy (Eq. 10) plotted as a function of Δr_{OH}. When $\beta = 1$, the local energy is constant. For the narrower ϕ_{T}, the local energy diverges at larger Δr_{OH} values. As β is increased, the local energy converges to the potential energy. (C) ψ^2 obtained from DMC simulations using the ϕ_{T} shown in panel A. (D) The drift term (Eq. 11) plotted as a function of Δr_{OH}. For the narrower ϕ_{T} the drift term picks up a larger slope at large Δr_{OH} values, whereas when ϕ_{T} is broadened the drift term shows a weaker dependence on Δr_{OH}. In the limit of a constant trial wave function, the drift term is 0. Additional details about how these calculations were preformed are provided in Appendix SA.

2.4 Choice of guiding functions - one-dimensional examples

The above description outlines guided DMC simulations, in which $\Phi_{\rm T}$ provided the guiding function. This function has the effect of favoring configurations in which the amplitude of $\Phi_{\rm T}$ is large, and, through the drift term, shifting walkers that are in regions of configuration space where $\Phi_{\rm T}$ is small toward geometries where $\Phi_{\rm T}$ is larger. As will be discussed below, the benefit of this approach is that it greatly improves the efficiency of the algorithm when $\Phi_{\rm T}$ is well-defined, but, in cases where $\Phi_{\rm T}$ is poorly chosen, the guiding functions can over-constrain the wave function, leading to inaccurate results. An alternative approach is to use unguided DMC, in which $\Phi_{\rm T}$ is constant. Substituting this form for $\Phi_{\rm T}$ into the above expressions, we find that the changes in the approach reflect,

$$\begin{aligned} E_{\rm L}(\mathbf{x}) &= V(\mathbf{x}) \\ \mathbf{D}(\mathbf{x}) &= 0 \\ \mathcal{P} &= 1 \end{aligned}$$

With these changes, we recover the unguided DMC approach, which was described by Anderson,[32, 41] and reviewed elsewhere.[34]

More generally, the guiding function is chosen either as an approximation to the wave function of the state of interest, or as a way to constrain the walkers to ensure that the system does not dissociate. The goal in selecting a guiding function is to obtain an improved sampling of the relevant configurations without imposing constraints on the sampled geometries, which limits the sampling of configurations where Ψ has amplitude.

To illustrate the advantages as well as the dangers in selecting a guiding function, we will focus on a one-dimensional model of an OH stretching vibration in water. This potential is plotted as a function of the displacement of the OH bond length, $r_{\rm OH}$, from its equilibrium value, $r_{{\rm OH},e}$, with the black dashed line in Figure 1B. We evaluated the ground state wave function based on this potential in a Discrete Variable Representation (DVR),[61] and plotted it with the thick green line in Figure 1A. The details of these calculations are provided in Appendix SA. Because these one-dimensional guiding functions will later be used in constructing guiding functions for larger systems, we will refer to them as $\phi_{\rm T}$, while the corresponding ground-state solution to this one-dimensional Hamiltonian will be represented by ψ. We also consider the behavior of the local energy and the drift term when the width of this wave function is multiplied by β, where β ranges from 0.60 to 1.40. These are shown with solid lines with various colors. The results when the guiding function is constant are shown with the black dashed line.

In Figure 1B, we explore how the local energy (defined in Eq. 10) changes as we alter the width of the guiding function, $\phi_{\rm T}$. For all of these calculations, we use the one-dimensional potential shown as a black dashed line in Figure 1B. When we use the wave function that is the ground state solution to this Hamiltonian (green thick line in panel A), the local energy is constant as $\hat{H}\phi_{\rm T}(\Delta r_{\rm OH})/\phi_{\rm T}(\Delta r_{\rm OH})$ is the ground state energy. At the other limit, when $\phi_{\rm T}$ is constant, the local energy is the same as the potential energy, as is shown with the black dashed lines in Figure 1B. As $\phi_{\rm T}$ is made wider (blue and purple curves), the shape of the $E_{\rm L}(\Delta r_{\rm OH})$ curve is intermediate between the constant value that is obtained when the green guiding function is used, and the potential energy. On the other hand, making $\phi_{\rm T}$ narrower causes the local energy to become negative as $\Delta r_{\rm OH}$ increases (see the red and gold curves). This has the desired effect of moving amplitude into regions where ψ has amplitude, but $\phi_{\rm T}$ has become small. It also leads to poor behavior of the DMC simulation and results in errors in the calculation of the

ground state energy. For example, when the ϕ_T guiding functions with $\beta = 0.6$ and 0.8 are used, the calculated zero point energies are too large by 7 and 114 cm^{-1}, respectively, while energies obtained using the other three ϕ_T or an unguided DMC simulation are within 2 cm^{-1} of the expected energy (see Appendix SB). We will refer to this problem as one of an over-constrained wave function in the following discussion.

The second quantity we consider is the drift term, shown in Figure 1D. Again focusing on the two limiting behaviors, when ϕ_T is constant, the drift term is zero. When ϕ_T is not constant, the drift term becomes negative at positive values of Δr_{OH}, and positive for negative values of Δr_{OH}. In this way, the drift term causes walkers to be shifted toward 0, where the ϕ_T all have maxima. The slope of the drift term increases as the ϕ_T becomes narrower, causing the walkers to accumulate in the values of Δr_{OH} where the local energy is large.

Despite the differences between the widths of the ϕ_T and the resulting potential and drift terms, the probability amplitude obtained from DMC calculations shown in Figure 1C show much less variability. In fact, with the exception of the narrowest ϕ_T, the plots of ψ^2 based on DMC simulations using these inputs are virtually indistinguishable.

2.5 Choice of guiding functions - molecular systems

The above discussion focused on a one-dimensional model system. While the insights gained from this system aid in considering appropriate forms for Φ_T for higher dimensional systems, the higher dimensionality provides opportunities for multiple strategies. One approach, which parallels strategies taken in electronic structure, employs Vibrational Self-consistent Field (VSCF) approaches, in some cases augmented by a small vibrational configuration interaction (VCI) calculation. Such an approach was employed by Bulik, Frisch, and Vaccaro for studies of the ground and excited states of H_2O, H_3^+, and their deuterated isotoplogues.[62] While such an approach is effective, the calculation of the guiding function itself can be demanding and will not necessarily scale well to larger systems. We recently explored an alternative approach, in which we used the harmonic ground state wave function as a guiding function to describe the same systems.[63] We found that this approach both worked well and is amenable to generalization to larger molecules.

Following approaches taken in the electronic structure community, where Jastrow factors are commonly employed,[64] Schmidt and co-workers[65, 66, 67] employed this form of guiding functions in studies of diatomic molecules with several rare gas atoms. More recently Huang, *et al* [68] and Acioli and co-workers [69, 53] followed a similar approach in which they developed parameterized guiding functions, the parameters of which were determined using variational Monte Carlo (VMC) calculations. In their work, Acioli and co-workers employed guiding functions that are expressed as $\prod_{i,j} \exp\left[\Delta S_i A_{ij} \Delta S_j\right]$, where ΔS_i represents the displacement of an atom-atom distance from its equilibrium value, and the A_{ij} represent the parameters that are optimized in the VMC calculation. In this way, the guiding function has many of the characteristics of the ground state wave function in a harmonic approximation. This approach has been used by Acioli, Xie, Braams, and Bowman in a study of H_5^+.[53] Similarly, Cho, Singer, and coworkers implemented a coupled, full-dimensional internal coordinate guiding function for DMC simulations of $H_5O_2^+$.[68] Another strategy was taken by Guaediola and Navarro,[70] Sola and Boronat,[71] and later by Kohno and Mandelshtam [72] in which they used various combinations of one, two, and three-body guiding functions to confine the relative orientation and interaction of H_2 in para-hydrogen clusters. The later work of Kohno and Mandelstham demonstrated that

the use of such functions may lead to biases in the hydrogen cluster wave function, particularly in the radial distribution of H_2 groups, relative to unguided simulations. In another study, Mallory and Mandelstham comment that the use of such a form of the guiding function in a system with multiple accessible minima on the potential energy surface may overly constrain the simulation [73].

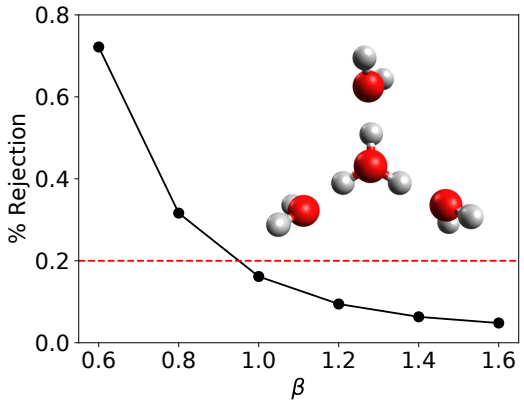

Figure 2: Average percentage of walkers where the attempted displacement was rejected based on the Metropolis step, plotted as a function of β. Here, β provides the width of the $\varphi(r_{\mathrm{OH}})$ functions (see Figure 1) used to construct Φ_{T} in Eq. 19. These results are based on a simulation of $H_9O_4^+$ (shown in the inset) with $40\ 000$ walkers. The red dashed line shows the target value of 0.2 %. Additional details about this simulation and the numerical values of the plotted points are provided in Appendix SA and SB, respectively.

In a recent series of studies, we proposed an alternative approach for developing guiding functions for studies of molecular clusters. In recognition of the pitfalls of trying to describe the intermolecular interactions with guiding functions, while realizing that often the intramolecular vibrations are only weakly perturbed by the interactions with other molecules, we chose to focus on the intramolecular degrees of freedom in developing the guiding functions. In addition, we chose to express the guiding function as a product of functions that depend on only one of the vibrational degrees of freedom. For example, for water clusters, one can imagine using the ground state solution to the one-dimensional OH stretch potential, shown in green in Figure 1A and B, to describe each of the OH stretching vibrations, $\phi(r_{\mathrm{OH}})$ and a harmonic approximation to the one-dimensional bend function, $\chi(\theta_{\mathrm{HOH}})$. In this way, for a cluster comprised of M water molecules,[48, 74]

$$\Phi_{\mathrm{T}}(\mathbf{r}_{\mathrm{OH}}, \theta_{\mathrm{HOH}}) = \prod_{l=1}^{M} \phi_{\mathrm{T}}(r^{(l)}_{\mathrm{OH},1}) \phi_{\mathrm{T}}(r^{(l)}_{\mathrm{OH},2}) \chi_{\mathrm{T}}(\theta^{(l)}_{\mathrm{HOH}}) \tag{19}$$

This approach is unlikely to lead to problems associated with guiding functions introducing unphysical constraints on the width of the wave function because the range of equilibrium OH bond lengths and HOH angles in the cluster environment is an order of magnitude smaller than the widths of the corresponding wave functions. A similar strategy was proposed by Suhm and Watts,[39] and we have found this approach to be very effective for studies of these cluster systems.[40, 48, 74]

This weak dependence of the equilibrium bond length or the width of the ground state wave function on the cluster environment is not expected to apply to all systems. For example in the protonated water clusters, when the hydronium ion is solvated by water moleclues the OH bond lengths in the hydronium core depend strongly on the distance between the oxygen atoms in the hydronium and solvating water molecule.[26] We have found that we could generalize the above approach to these situations by allowing the center and width of the guiding function, described by Eq. 19, to depend on other internal coordinates, in this case the OO distance. Details of this strategy are described elsewhere.[40]

A challenge in using these multi-dimensional guiding functions comes in determining when they are performing well. While the behavior of the local energy and drift term provide insights into the appropriateness of a choice of ϕ_{T} for the one-dimensional system in Figure 1, it can be challenging to extend this analysis to a multi-dimensional system. Another measure of the behavior of the simulation is provided by the fraction of the attempted moves that are rejected in the Metropolis step. As noted above, we aim for this value to be no larger than 0.2%, as indicated by the red dashed line in Figure 2. In Figure 2, we show the average percentage of the attempted moves that are rejected in a simulation of $H_9O_4^+$ (see inset in Figure 2), and explore how the number of rejected moves is affected by the width of the contribution to Φ_{T} that describes the OH stretching vibrations of the outer water molecules. For all of the Φ_{T} a harmonic function is used to describe the bending vibrations of the outer water molecules (See Ref. [40] for additional details). As can be seen, for $\beta \geq 1$, the rejection fraction remains smaller than 0.2%, and this value approaches zero with increasing values of β. This is consistent with the fact that when Φ_{T} is constant, none of the moves will be rejected. For the narrower ϕ_{T} ($\beta < 1$), the fraction of rejected moves increases. In this way, the fraction of rejected moves provides a straightforward way to assess when the guiding function is over-constrained.

3 Evaluating properties using DMC

While the ability to evaluate the ground state wave function and zero-point energies are both very powerful, these two quantities alone are quite limiting. One of the powerful aspects of DMC is that it provides a general approach for the evaluation of the ground state wave function, from which we can obtain the probability amplitude, and from that evaluate various properties or explore couplings among vibrations. This capability is valuable, as often the systems that are explored using DMC are ones that are not accessible by basis set calculations due to the large number of vibrational degrees of freedom and the lack of a good zero-order description for large amplitude vibrations.

There are several approaches that can be used to obtain the probability amplitude, and we will focus on three, which have been used in studies of molecular vibrations. Examples include molecular ions like H_5^+,[75] CH_5^+,[76, 77] and $H^+(H_2O)_n$.[27, 78, 79]

3.1 Using f to obtain properties

In guided DMC, we obtain a Monte Carlo sampling of

$$f(\mathbf{x}) = \Psi(\mathbf{x})\Phi_{\mathrm{T}}(\mathbf{x}) \tag{20}$$

which allows us to evaluate matrix elements of multiplicative operators over Φ_{T} and Ψ using

$$\langle \Phi_{\mathrm{T}}|O|\Psi\rangle = \sum_i w_i(\tau) O\left(\mathbf{x}_i(\tau)\right) \tag{21}$$

where the evaluation is based on the positions and weights of the walkers at time τ. If Φ_{T} is a good approximation to Ψ, Eq. 21 should provide a good approximation to $\langle \Psi|O|\Psi\rangle$. Barnett, Reynolds and Lester [80] as well as Cho and Singer [68] showed that this approximation to Ψ^2 can be improved by recognizing that since Φ_{T} is expected to be a good approximation to Ψ, Ψ can be expressed as as

$$\Psi = \Phi_{\mathrm{T}} + \epsilon \tag{22}$$

where ϵ represents the small difference between Ψ and Φ_{T}, and

$$\Psi^2 = 2f - \Phi_{\mathrm{T}}^2 - \epsilon^2 \approx 2f - \Phi_{\mathrm{T}}^2 \tag{23}$$

Based on Eq. 19 we approximate Φ_{T} by a product of one-dimensional functions. If O in Eq. 21 is a function of coordinates on which Φ_{T} depends (e.g. the the OH bond lengths or the HOH angles), Eq. 23 allows for straightforward evaluation of $\langle \Psi|O|\Psi\rangle$. On the other hand, such an approach is not expected to be as effective for analyzing properties of the intermolecular degrees of freedom. It also introduces bias as it still relies on Φ_{T} being a good approximation to Ψ.

3.2 Adiabatic DMC

A second approach is based on the finite field approach in electronic structure,[81] which provides an avenue for obtaining expectation values of operators when one can evaluate the energy of a quantum state, but does not have access to the wave function. This approach is based on perturbation theory, in which

$$H' = H + \lambda W \tag{24}$$

and

$$E_0 = \sum_n \lambda^n E_0^{(n)} \tag{25}$$

where,

$$E_0^{(1)} = \langle \Psi_0|W|\Psi_0\rangle \tag{26}$$

In contrast to typical perturbation theory, in Eq. 24 the Hamiltonian for the system of interest is given by H, while the operator we want to evaluate the expectation value of is given by W. Additionally, while we can evaluate the ground state energy for H' for any value of λ, we do not have direct access to Ψ^2.

In the adiabatic DMC (ADMC) approach, a DMC simulation is equilibrated based on H' with a chosen value of λ. Once equilibrated, the simulation is run for additional time steps, where at each time step the value of λ is increased by a small amount, $\delta\lambda$. The value of $\delta\lambda$ is chosen to be sufficiently small such that the ensemble remains equilibrated throughout the simulation. More quantitatively, the shift in the ground state energy with a change of $\delta\lambda$ should be small compared to the size of the statistical fluctuations of E_{ref}.

At the end of the simulation, $E_0(\lambda)$ is fit to a low order polynomial in λ. The intercept provides the energy of the unperturbed Hamiltonian while the first derivative at $\lambda = 0$ is equated to $\langle W\rangle$. Comparison of the $\lambda = 0$ energy obtained from the ADMC simulation to that from a standard

DMC simulation provides a way to calibrate the accuracy of the ADMC results. As with standard DMC simulations, this procedure is repeated several times to obtain an average and standard deviation among the calculated results. Additional details and examples of this approach can be found elsewhere.[82, 83, 84, 85] The above approach, while very accurate is not particularly efficient as each expectation value requires a separate DMC simulation to evaluate. On the other hand, it provides an excellent way to benchmark other, more efficient approaches.

3.3 Descendent weighting

A third approach, termed descendent weighting, was described by Suhm and Watts [39] and the following discussion is based on the description presented by Barnett, Reynolds and Lester.[80] The idea comes from the observation that the DMC simulation provides a sampling of $f = \Psi\Phi_{\mathrm{T}}$, evaluating the expectation value of a multiplicative operator, $O(\mathbf{x})$, using the Monte Carlo sampling of f requires us to multiply $O(\mathbf{x})$ by $\Psi(\mathbf{x})/\Phi_{\mathrm{T}}(\mathbf{x})$ as

$$\frac{\langle\Psi|O|\Psi\rangle}{\langle\Psi|\Psi\rangle} = \frac{\langle\Phi_{\mathrm{T}}|O\times(\Psi/\Phi_{\mathrm{T}})|\Psi\rangle}{\langle\Phi_{\mathrm{T}}|(\Psi/\Phi_{\mathrm{T}})|\Psi\rangle} = \frac{\langle\Phi_{\mathrm{T}}|O\times(\Psi/\Phi_{\mathrm{T}})\times\langle\Phi_{\mathrm{T}}|\Psi\rangle|\Psi\rangle}{\langle\Phi_{\mathrm{T}}|(\Psi/\Phi_{\mathrm{T}})\times\langle\Phi_{\mathrm{T}}|\Psi\rangle|\Psi\rangle} \tag{27}$$

To start, we assume that at $\tau = 0$, our distribution is localized at the coordinates described by $\mathbf{x}'$

$$f_{\mathbf{x}'}(\mathbf{x},0) = \Phi_{\mathrm{T}}(\mathbf{x})\Psi(\mathbf{x},0) = \delta(\mathbf{x}-\mathbf{x}') \tag{28}$$

where we can expand $\Psi(\mathbf{x},0)$ in the eigenstates of the Hamiltonian in Eq. 4 as

$$\delta(\mathbf{x}-\mathbf{x}') = \Phi_{\mathrm{T}}(\mathbf{x})\sum_n c_n\varphi_n(\mathbf{x}) \tag{29}$$

Multiplying by $\varphi_{n'}(\mathbf{x})/\Phi_{\mathrm{T}}(\mathbf{x})$ and integrating over $\mathbf{x}$ we find that

$$c_{n'} = \frac{\varphi_{n'}(\mathbf{x}')}{\Phi_{\mathrm{T}}(\mathbf{x}')} \tag{30}$$

Propagating $f_{\mathbf{x}'}$ to long times

$$f_{\mathbf{x}'}(\mathbf{x},\tau) = c_0\Phi_{\mathrm{T}}(\mathbf{x})\varphi_0(\mathbf{x})e^{-(E_0-E_{\mathrm{ref}})\tau} \tag{31}$$

Since at large τ, $\Psi = \varphi_0$, we substitute Ψ for φ_0 in Eq. 31. Finally, by integrating over $\mathbf{x}$ and using Eq. 30 to evaluate c_0, the asymptotic population,

$$\begin{aligned} P(\mathbf{x}') &= \int f_{\mathbf{x}'}(\mathbf{x})d\mathbf{x} \\ &= \left(\frac{\Psi(\mathrm{x}')}{\Phi_{\mathrm{T}}(\mathrm{x}')}\right)e^{-(E_0-E_{\mathrm{ref}})\tau}\langle\Phi_{\mathrm{T}}|\Psi\rangle \end{aligned} \tag{32}$$

Rearranging Eq. 32,

$$\left(\frac{\Psi(\mathrm{x}')}{\Phi_{\mathrm{T}}(\mathrm{x}')}\right) = P(\mathbf{x}')e^{+(E_0-E_{\mathrm{ref}})\tau}\langle\Phi_{\mathrm{T}}|\Psi\rangle^{-1} \tag{33}$$

The above discussion focuses on a single δ-function. The procedure can be applied to an ensemble of δ-functions, represented by g in Eq. 8, resulting in

$$P(\mathbf{x}_j) \propto w_j(\tau+\tau_{\mathrm{DW}})/w_j(\tau) \tag{34}$$

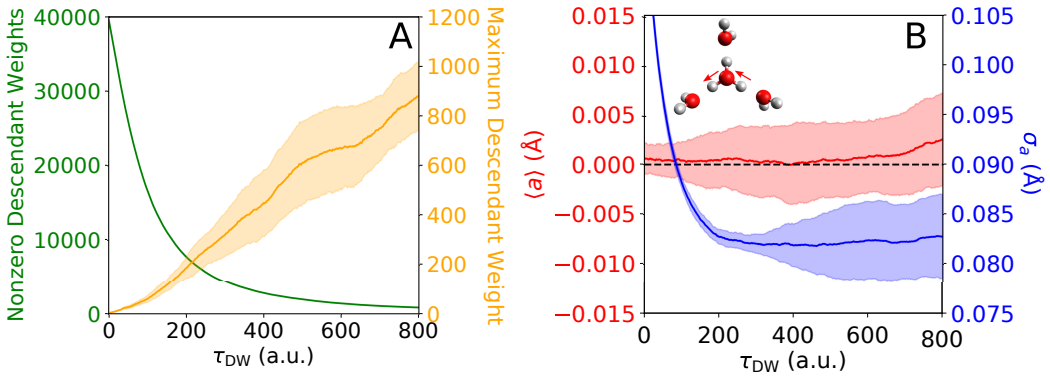

Figure 3: (A) Analysis of the distribution of descendent weights at the end of the descendent weight process, plotted as a function of the time over which weights are collected, τ_{DW}. The number of walkers that have descendant weights that are non-zero is plotted in green, while the maximum value of the descendant weights is shown in gold. (B) The expectation value of $a = (r_{\mathrm{OH}_1} - r_{\mathrm{OH}_2})/\sqrt{2}$ (red), illustrated with red arrows in the inset, and the standard deviation of a, σ_a (Eq. 36, blue), plotted as functions of τ_{DW}. The black dashed line provides the expected value of $\langle a \rangle$, which is 0 by symmetry. In both panels, the shaded regions provide one standard deviation based on five independent simulations. The results shown in this figure are based on guided DMC simulations of $H_9O_4^+$ with 40 000 walkers using discrete weights and Φ_{T} in Eq. 19 based on the wave function for the OH stretches that is obtained when $\beta = 1$, which is plotted in green in Figure 1A. See Appendix SA for additional details.

With this in mind, substituting the expression for $(\Psi(\mathrm{x}')/\Phi_{\mathrm{T}}(\mathrm{x}'))$ given by Eq. 33 into Eq. 27 gives

$$\begin{aligned}
\frac{\langle \Psi|O|\Psi\rangle}{\langle \Psi|\Psi\rangle} &= \frac{\langle \Phi_{\mathrm{T}}|O \times P|\Psi\rangle}{\langle \Psi|P|\Psi\rangle} \\
&= \frac{\sum_j \left(w_j(\tau+\tau_{\mathrm{DW}})/w_j(\tau)\right) \times w_j(\tau) O(\mathbf{x}_j)}{\sum_j \left(w_j(\tau+\tau_{\mathrm{DW}}/w_j(\tau)\right) \times w_j(\tau)} \\
&= \frac{\sum_j w_j(\tau+\tau_{\mathrm{DW}}) O(\mathbf{x}_j)}{\sum_j w_j(\tau+\tau_{\mathrm{DW}})}
\end{aligned} \tag{35}$$

The accuracy of the descendent weighting approach is sensitive to the choice of τ_{DW}, the amount of time over which the weights are collected. If τ_{DW} is too small $w_j(\tau+\tau_{\mathrm{DW}})/w_j(\tau)$ will not provide a good approximation to $\Psi^2(\mathbf{x}_j)$, while the sampling deteriorates as τ_{DW} increases.[39, 43] The above expression assumes continuous weighting. If discrete weighting is used, then $w_j(\tau) = 1$, and $w_j(\tau+\tau_{\mathrm{DW}})$ provides the number of walkers that can be traced back to the jth walker at time τ.

This sensitivity of the results of the descendant weighting procedure to the value of τ_{DW} is illustrated by the results plotted in Figure 3, which are based on calculations of ground state properties of $H_9O_4^+$ in which the discrete weighting scheme, described above, was used. In Figure 3A, we plot the number of walkers for which the value of $w_j(\tau+\tau_{\mathrm{DW}})$ is non-zero in

green. As can be seen the number of walkers for which $w_j(\tau + \tau_{\mathrm{DW}})$ is non-zero decreases roughly exponentially as a function of propagation time, starting from a situation where all of the weights are equal to one. Since the sum of the weights remains roughly constant, as the number of walkers with non-zero weights decreases, the value of the largest weight increases. This is shown with the gold line, and the yellow shading provides the standard deviation among five independent DMC simulations. This behavior is reflected in the calculation of the average value of the asymmetric stretch coordinate, a plotted in red in Figure 3B with the vibration shown with red arrows in the inset. In this plot we also show the width of the projection of the probability amplitude onto this coordinate,

$$\sigma_a = \sqrt{\langle \Psi | a^2 | \Psi \rangle - \langle \Psi | a | \Psi \rangle^2} \tag{36}$$

in blue. For comparison, the expected value based on symmetry for $\langle a \rangle$ is provided with a black dashed line. As is seen, in the plots, the longer the descendant weights are collected, the larger the range of results that are obtained. On the other hand for $\tau_{\mathrm{DW}} < 200$ a.u. the value of σ_a is not converged. There is a limited range of τ_{DW} for which the values appear to be converged and the simulation to simulation variation remains small. For most of the systems we have studied, we have found that a value of τ_{DW} of approximately 250 a.u. provides good results.

3.4 Evaluating matrix elements

The above discussion focused on the evaluation of expectation values of primarily multiplicative operators. One can also use DMC to obtain matrix elements involving wave functions that describe two different states of the system of interest, assuming that one can use DMC to evaluate both states. Approaches for evaluating excited states will be described in the following section. For now, we assume that we can calculate $f_i = \Phi_{\mathrm{T}}^{(i)} \Psi^{(i)}$ for the ith vibrational state of the system of interest. Following the discussion above, and as described by Barnett *et al.* [86] and by us [63, 87] just as one can use f to obtain Ψ^2 by following Eq. 23, we can approximate $\Psi^{(i)}\Psi^{(i')}$ using

$$\Psi^{(i)}\Psi^{(i')} \approx f^{(i)} \left(\frac{\Phi_{\mathrm{T}}^{(i')}}{\Phi_{\mathrm{T}}^{(i)}} \right) + f^{(i')} \left(\frac{\Phi_{\mathrm{T}}^{(i)}}{\Phi_{\mathrm{T}}^{(i')}} \right) - \Phi_{\mathrm{T}}^{(i)} \Phi_{\mathrm{T}}^{(i')} \tag{37}$$

Likewise, by analogy to using Eq. 35 to obtain an expectation value based on descendant weights, we can take the ensemble at τ that is based on a simulation for the state $\Psi^{(i)}$, and propagate it forward by τ_{DW} using $\Phi_{\mathrm{T}}^{(i')}$ for the guiding function. This allows us to generate descendent weights for the i'th state, $w_j^{(i' \leftarrow i)}(\tau + \tau_{\mathrm{DW}})$. Using these weights,

$$\frac{\Psi^{(i')}(\tau)}{\Phi_{\mathrm{T}}^{(i')}(\mathbf{x}_j)} = \frac{w_j^{(i' \leftarrow i)}(\tau + \tau_{\mathrm{DW}})}{w_j^{(i)}(\tau)} \tag{38}$$

and

$$\left\langle \Psi^{(i)}|O|\Psi^{(i')}\right\rangle = \left[\sum_j w_j^{(i'\leftarrow i)}(\tau+\tau_{\rm DW})O(\mathbf{x}_j)\left(\frac{\Phi_{\rm T}^{(i')}(\mathbf{x}_j)}{\Phi_{\rm T}^{(i)}(\mathbf{x}_j)}\right)\right] \times\left[\sum_j w_j^{(i)}(\tau+\tau_{\rm DW})\right]^{-1/2} \times\left[\sum_j \left(w_j^{(i'\leftarrow i)}(\tau+\tau_{\rm DW})\right)^2\left(w_j^{(i)}(\tau+\tau_{\rm DW})\right)^{-1}\left(\frac{\Phi_{\rm T}^{(i')}(\mathbf{x}_j)}{\Phi_{\rm T}^{(i)}(\mathbf{x}_j)}\right)^2\right]^{-1/2} \quad (39)$$

4 Excited States

4.1 Fixed-node approaches

The above discussion focused on the evaluation of the ground state solution to the vibrational Schrödinger equation. In contrast to electronic structure problems, where the nodal surface is a complicated function of the electronic coordinates, the nodal surface for states with low-levels of vibrational excitation can be described by a $3N-7$ dimensional hyperplane, which is defined by the values of one of the coordinates at which the wave function is zero. This approach requires a careful choice of vibrational coordinates, and is based on the idea that for low levels of vibrational excitation, the excitation is localized in a single oscillator. We have validated this strategy through DMC calculations of all of the $v=1$ levels of Ne_2·SH, Ne_2·OH [88] and $H_3O_2^-$,[89] where the results were compared to those obtained by basis set approaches. The approach has also been used to evaluate selected excited states of $H_5O_2^+$ and H_5^+.[18, 75, 78, 90] Although the excited states are evaluated by assuming that the position of the node depends on the value of a single vibrational coordinate, the wave function is still fully coupled, as is illustrated for the wave function for the vibrationally excited state of H_5^+ shown in Figure 4. In this calculation, nodes are placed when R_1 or $R_2 = 1.3666$ Å (see insert to Figure 4 for definitions of R_1 and R_2).[75] As seen in the projection, the amplitude does not align along a line where $R_1+R_2=\text{constant}$ as would be expected for a separable wave function. Rather, it displays significant curvature.

Once the nodal surface has been determined, the excited states may be evaluated using one of two approaches. If $\Phi_{\rm T}$ is a function of the coordinate that is being excited, ensuring that $\Phi_{\rm T}$ has the desired nodal structure will provide the excited state of interest. This is an area of current exploration in our lab. If $\Phi_{\rm T}$ does not depend on the coordinate along which the molecule is being excited or when preforming an unguided DMC simulation, one can introduce a node by modifying the potential to make it infinite where the amplitude of the wave function is negative to obtain the part of the wave function with positive amplitude. Repeating the procedure, making the potential infinite in the region where the amplitude of the wave function is positive provides the part of the wave function with negative amplitude.[41] By making the potential infinite where the amplitude of the wave function is expected to be negative forces the wave function to be zero in that region of configuration space as the weight of a walker that moves into a region of infinite potential will become vanishingly small and the walker will be removed from the simulation during the branching process described above. Mathematically,

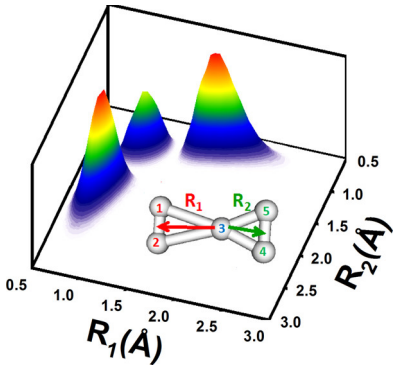

Figure 4: The DMC probability amplitude of H_5^+ with two quanta of excitation in the shared proton stretch. For this simulation, the wave function is required to go to zero when R_1 or $R_2 = 1.3666$ Å as described in Ref. [75]. Reprinted with permission from Ref. [75]. Copyright 2013 American Chemical Society

the behavior of a wave function near a node and near an infinite potential barrier are the same in so far as it approaches zero with finite slope. While the introduction of a node in this way is straightforward, because the simulation is performed with finite time steps we need to account for the possibility that in a single time step, a walker that appears to have remained on the same side of the nodal surface could have crossed the node and crossed back had a smaller value of $\Delta\tau$ been used for the simulation. Following Anderson,[41] and by analogy to Eq. 15, the probability of this happening is given by

$$\mathcal{P}_{\text{recross}} = \frac{P(q \to q')}{P(q \to -q')} = \frac{\exp\left(-\left(q'-q\right)^2/2\sigma_q^2\right)}{\exp\left(-\left(-q'-q\right)^2/2\sigma_q^2\right)} = \exp\left(-\frac{4qq'}{2\sigma_q^2}\right) \tag{40}$$

where $q = r - r_{\text{node}}$ represents the coordinate along which the node is placed, where the node is at $q = 0$. Since the position of the node depends on only one coordinate, the distance of the walker from the node is given by the value of q. Additionally, $\sigma_q = \hbar\sqrt{\Delta\tau G_{qq}}$ where G_{qq} is the diagonal Wilson G-matrix element [91] in q. As with the Metropolis step, $\mathcal{P}_{\text{recross}}$ is compared to a random number from a uniform distribution on the $[0, 1]$ domain. If the random number is smaller than $\mathcal{P}_{\text{recross}}$, the walker is assumed to have crossed the node, and its weight is set to zero. While the treatment of the recrossing correction is essential to obtain accurate results from an unguided excited state calculation, in a guided DMC simulation, the drift term diverges at the node, so amplitude should not accumulate near the node.[87]

The above discussion assumes that the position of the nodal surface is known. For excitation of a vibration that is not totally symmetric, the node in the first excited state will occur when the associated coordinate is zero. When the vibration that is being excited is totally symmetric or when a higher excited state is being considered, the location of the node requires additional consideration. Drawing from the work of Buch and co-workers,[92, 93] we note that when the node is properly placed, the energies calculated for the parts of the wave function with positive and negative amplitude will be identical. This observation provides a way to identify the position of the nodal surface. Following the discussion of the adiabatic DMC approach for evaluating expectation values,[34, 82, 84, 85] a similar approach can be used to identify the position of

the nodal surface. Specifically, a pair of DMC simulations are performed, one for the part of the wave function that has positive amplitude and one for the region with negative amplitude. During the simulation, the position of the nodal surface is slowly shifted, making the energies that are evaluated functions of the position of the node. When the node is not properly placed, one energy will be too high, while the other is too low. By fitting the two curves that describe the energy as a function of the position of the node to low order polynomials and finding the value of the coordinate at which the two curves cross, we have a way to evaluate both the optimal position of the node and the associated excited state energy.

4.2 Ground state probability amplitude approximation

While the fixed node approach provides an effective method for calculating the energies and wave functions for states with one or two quanta of excitaiton, it is expensive as sets of independent DMC simulations need to be run for each nodal region for each excited state of interest. On the other hand, we know that considerable information is encoded in the ground state wave function. In a second approach, which we call the Ground State Probability Amplitude (GSPA) approximation we analyze the ground state probability amplitude to obtain transition energies and intensities for tranitions involving one or two quanta of excitation.[79, 94, 95] In this way only the ground state DMC calculation is needed to obtain the spectrum.

The GSPA approximation is based on the observation that for many one-dimensional model problems, excited state wave functions can be expressed as the product of the ground state wave function and a polynomial. The coefficients in the polynomial are chosen to ensure orthogonality with the ground state. For example the nth excited state of a harmonic oscillator is the product of the nth Hermite polynomal and the ground state wave function. In this way,

$$\Psi_{n_v=1,n_w=1} = (q_v - q_v^0)(q_w - q_w^0)\Psi_0 \tag{41}$$

and

$$\langle \Psi_{n_v=1,n_w=1}|V|\Psi_{n_v=1,n_w=1}\rangle = \langle \Psi_0| \left[(q_v - q_v^0)(q_w - q_w^0)\right]^2 V|\Psi_0\rangle \tag{42}$$

while

$$\langle \Psi_{n_v=1,n_w=1}|\vec{\mu}|\Psi_0\rangle = \langle \Psi_0|(q_v - q_v^0)(q_w - q_w^0)\vec{\mu}|\Psi_0\rangle \tag{43}$$

were $\vec{\mu}$ is the dipole moment, and the intensity

$$\begin{aligned} I_{n_v=1,n_w=1\leftarrow 0} &\propto \nu_{n_v=1,n_w=1\leftarrow 0}\langle \Psi_{n_v=1,n_w=1}|\vec{\mu}|\Psi_0\rangle^2 \\ &\approx \nu_{n_v=1,n_w=1\leftarrow 0}\langle \Psi_0|(q_v - q_v^0)(q_w - q_w^0)\vec{\mu}|\Psi_0\rangle^2 \end{aligned} \tag{44}$$

As can be seen, within the GSPA approximation the matrix elements in Eqs. 41 and 42 can be evaluated as expectations over the ground state probability amplitude. The evaluation of the expectation value of the kinetic energy operator, $\langle T\rangle$, is less obvious as it requires derivatives with respect to the internal coordinates. On the other hand, we can utilize the relationships between $\langle p^2\rangle$ and $\langle q^2\rangle$ for the harmonic oscillator to develop approximate expressions for $\langle T\rangle$ in terms of expectation values of q^n.[79, 94]

With the above relationships, the only remaining challenge is to define the coordinates. This is achieved by identifying the eigenvectors of the matrix of mass-weighted second moments of the ground state probability amplitude, evaluated based on a well-chosen set of internal coordinates. In the limit of a harmonic potential, this procedure will recover the usual normal modes. For anharmonic systems, the use of the probability amplitude rather than the potential

to define the normal modes allows us to account for some of the higher order couplings in these systems. Additional details of the approach can be found in our earlier studies, particularly Ref. [79]. In that work, we showed that the results of the GSPA approach provides spectra for $H_3O_2^-$,[94] $H_5O_2^+$,[95] $H_7O_3^+$, and $H_9O_4^+$ [79] that are in good agreement with other approaches, specifically the VSCF/VCI approach coded in the MULTIMODE program developed by Bowman and co-workers [96] and fixed-node DMC calculations.

5 Convergence properties of guided and unguided DMC simulations

As mentioned above, DMC is a powerful tool because it allows us to obtain a full-dimensional wave function for the molecule of interest based on the potential surface for that molecule. The wave function can be analyzed using the approaches described above to then obtain insights into the structure and spectroscopy of this molecule. On the other hand, as the size of the system of interest increases, the number of walkers required to converge the simulation increases. In the discussion that follows, we consider how a well-chosen guiding function can lead to both a reduction of the computational cost and an increase in the accuracy of the zero-point energy and the ground state wave function.

For the purposes of the following discussion, we will focus on $H_9O_4^+$, and in Figure 5, we explore how the size of the ensemble, which is provided by the number of walkers, N_w, and the choice of the guiding function affect the distribution of $E_{\rm ref}$ as a function of τ. Specifically the choice of the guiding function is characterized by the width of $\phi(r_{\rm OH})$ in Eq. 19, and the functions used to describe the $\phi_{\rm OH}$ are the one-dimensional $\phi_{\rm T}$ plotted in Figure 1A. In Figure 5A, we explore how the size of the ensemble used in the DMC simulation affects the size of the fluctuations of $E_{\rm ref}$, which is characterized by $\sigma_{E_{\rm ref}}$. Here $\sigma_{E_{\rm ref}}$ provides the standard deviation of the calculated values of $E_{\rm ref}$ when it is evaluated at every time step from $\tau = 5000$ a.u. to the end of a single DMC simulation. As can be seen in the results plotted in Figure 5A, the values of $\sigma_{E_{\rm ref}}$ range from approximately 560 cm^{-1} when the number of walkers in the simulation at $\tau = 0$ is 1000 to 90 cm^{-1} when $N_w = 40\ 000$. An unguided simulation with the same ensemble size displays a value of $\sigma_{E_{\rm ref}}$ that is roughly twice as large as its guided counterpart.

In order to calculate the zero-point energy from a DMC simulation, one averages the value of $E_{\rm ref}$ over a specified range of τ. The effect of the choice of the range of τ over which $E_{\rm ref}$ is averaged has been explored elsewhere.[43] In Figure 5B, we show the convergence of the calculated DMC zero-point energy of $H_9O_4^+$ as a function of N_w for several choices of guiding functions, which are characterized by the parameter, β, where β is proportional to the width of $\phi_{\rm OH}$ in Eq. 19. For these calculations, we ran five DMC simulations, and the plotted values provide the average of the zero-point energies, E_0, obtained from these simulations, while the error bars reflect one standard deviation among the five results. To differentiate the simulation to simulation changes in the time-averaged values of $E_{\rm ref}$ from the size of the fluctuations of the value of $E_{\rm ref}$ in a single simulation, we will refer to the standard deviations in the evaluation of E_0 as σ_{E_0}. In this plot, the black circle and line reflect results from an unguided simulation, while the results shown in green provide the results obtain from a guided DMC calculation based on $\phi_{\rm OH}$ with $\beta = 1$, plotted in green in Figure 1A. The results of additional DMC simulations with $N_w = 40\ 000$, which are based on the other forms of $\phi_{\rm OH}$ shown in Figure 1A, are also provided. These results are shown on an expanded scale in the inset. It is important to note

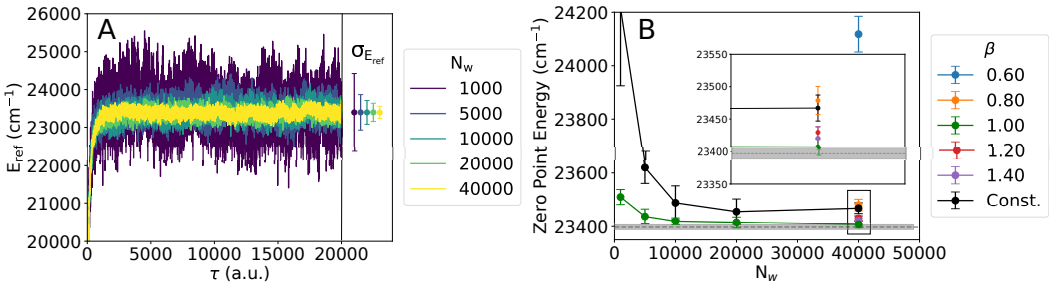

Figure 5: (A) E_{ref} plotted as a function of τ for different ensemble sizes (characterized by the number of walkers, N_w) for a single guided DMC simulation of $H_9O_4^+$ using the wave functions with $\beta = 1$ and shown in green in Figure 1A to describe the OH stretches. At the right, the average value of E_{ref} and its standard deviation based on these five calculations are provided. The values are obtained from the values of E_{ref} that are evaluated from $\tau = 5000$ a.u. to the end of the simulation at $20\ 000$ a.u. (B) The average values of E_{ref} from five independent simulations are summarized in the results plotted in green in this panel. This plot also provides the standard deviation based on these five simulations (error bars) and the corresponding results from unguided DMC simulations (Const., black). For these DMC simulations, E_{ref} was averaged from $\tau = 5000$ to $20\ 000$ a.u. For $N_w = 40\ 000$ walkers, guided DMC simulations were performed using Ψ_{T} that are based on the ϕ_{T} plotted in Figure 1A.The inset shows an expanded view of these results. The dotted line and the grey shaded region provide the calculated DMC E_0 and σ_{E_0} from a previous study of $H_9O_4^+$.[40] The details of these DMC calculations and the numerical values of $\sigma_{E_{\mathrm{ref}}}$, E_0 and σ_{E_0} are provided in Appendices SA and SB, respectively.

that while $\sigma_{E_{\mathrm{ref}}}$ for the 40 000 walker simulation is 90 cm^{-1}, σ_{E_0} based on five such simulations is only 11 cm^{-1}. In other words, the large statistical fluctuations in E_{ref} in a single DMC simulation are not reflected in the fluctuations among the calculated zero-point energies when we compare results of several simulations.

Analysis of the results plotted in Figure 5B shows that there is generally good agreement between the calculated zero-point energy obtained when $\beta \geq 1$. Also, as the width of ϕ_{OH} is increased from $\beta = 1$, the calculated zero-point energy shifts from the value obtained when $\beta = 1$ to the value obtained from the unguided simulation (indicated by Const., black symbols in Figure 5B). This should not be surprising as the unguided simulation represents the limit when the width of the guiding function becomes infinite. On the other hand, as the guiding function is narrowed, the calculated energy also increases, and when $\beta = 0.6$, the calculated zero-point energy of the system is approximately 700 cm^{-1} higher than when $\beta = 1$. Additionally, there is a 61 cm^{-1} difference between the zero point energies calculated from the guided ($\beta = 1$) and unguided DMC simulations. This difference has been attributed to the larger ensemble sizes needed to obtain accurate results from unguided DMC simulations.[40] In fact, if we perform a single very large ($N_w = 1\ 000\ 000$) DMC simulation of the ground state of $H_9O_4^+$, we obtain a value for E_0 of 23 405 cm^{-1}. This is 1 cm^{-1} smaller than the value of E_0 that is obtained from the guided DMC simulation with $N_w = 40\ 000$.

Like the energy, the quality of the wave function will be sensitive to the size of the ensemble.[97] In fact, it will be more sensitive to the ensemble size than the energy is, as an error in the wave

function of $O(\epsilon)$ leads to an error in the energy of $O(\epsilon^2)$. Previously, we found that using a guiding function to describe the OH stretches and HOH bends in the external water monomers of the protonated water trimer, $H_7O_3^+$, we were able to improve the convergence properties of the projection of the probability amplitude onto the degrees of freedom that were included in the definition of $\Phi_{\rm T}$ in Eq. 19 as well as for intermolecular degrees of freedom, which were not included in the definition of $\Phi_{\rm T}$.[40] To illustrate this, in Figure 6 we plot projections of the probability amplitude onto the umbrella vibration in $H_9O_4^+$. The thin lines each provide the projection of the probability amplitude based on the descendent weights from an ensemble of walkers at at a specific value of τ, while the thick black line provides the average of these distribution. For this analysis, the umbrella coordinate is defined as the angle between the vector along one of the OH bonds in the hydronium core and a vector pointing from the oxygen in hydronium to the center of the triangle defined by three unit vectors along the three OH bonds in hydronium (see inset in Figure 6). By using this definition, the value of $\theta_{\rm umb}$ is independent of the choice of the OH bond used in the analysis. The results shown in Figure 6A are obtained from a guided DMC simulation, while panel B provides the results of an unguided simulation. As can be seen, the reproducibility of the projections of the probability amplitude onto the umbrella coordinate is much improved for the guided simulation compared to the results based on the unguided DMC simulation even when the umbrella mode is not one of the vibrations that was incorporated into the guiding function. The improved convergence behavior of the guided DMC simulation is attributed to differences in the potential energy and local energy surfaces used in the unguided and guided DMC simulations.[40, 48] In using a guiding function to describe the high frequency vibrations, the local energy becomes less sensitive to the values of these vibrational coordinates compared to the potential energy, where small changes in the OH bond length have a large effect on the calculated energy.

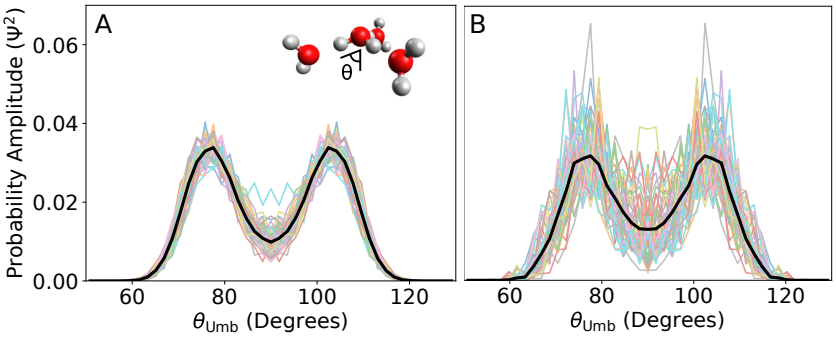

Figure 6: Projections of the ground state probability amplitude of for $H_9O_4^+$ onto the umbrella vibration (illustrated in the inset and described in the text) for (A) a guided DMC simulation based on $\phi_{\rm T}(r_{\rm OH})$ plotted in green in Figure 1A and (B) an unguided DMC simulation. The thin lines represent the probability amplitudes obtained from 50 ensembles of walkers, which were collected from five independent simulations with $N_w = 40\ 000$ every 1000 time steps starting at 10 000 a.u. The thick black curves provide the average of the 50 probability amplitudes.

6 Exploring the extent of proton transfer using DMC

The discussion so far focused on the DMC method, extensions and the effects of various parameters on the convergence behavior of a DMC simulation. The power of DMC comes in the fact that it allows us to explore properties of molecules or molecular clusters that undergo large amplitude motions. These are often questions that are difficult to explore by other methods.

To illustrate these capabilities, we focus on protonated water clusters with two to four water molecules. These ions have been studied extensively through vibrational spectroscopy as they are model systems for the study of the mechanism of proton transfer.[20, 25, 79, 98, 99, 100] One interesting aspect of these systems is the broad range of OH stretching frequencies that they display. In the case of $H_5O_2^+$, the excess proton is equally shared between the two water molecules, and the frequency of the vibration that is associated with the motion of this proton along the OO axis is 1085 cm^{-1}.[18] When one water molecule is added, the OH frequency of the hydrogen-bonded OH oscillators in the hydronium core becomes 2100 cm^{-1},[29] while the frequency of this vibration is further increased to 2650 cm^{-1} when a fourth water molecule is added.[27] This progression of frequencies has been attributed to the decrease in the proton delocalizaiton as water molecules are added to the system.[20, 26, 100] Since DMC allows us to interrogate the probability amplitude, it provides us the opportunity to quantify this effect.

In Figure 7, we plot projections of the ground state probability amplitude onto the distance between one of the solvated hydrogen atoms in the hydronium core and the oxygen in the hydronium core, O_1 shown with a black dot in the inset, and the distance between this hydrogen atom and the oxygen atom in the solvating water molecule, O_2 shown with the blue dot in the inset. These plots are based on the DMC calculations presented previously,[40] and are based on the potential surface of Yu and Bowman.[51] To determine the extent of proton transfer, we divide these plots into two regions, those for which $R_{O_2H} < R_{O_1H}$ where the proton is closer to the oxygen atom in the hydronium core and those for which $R_{O_2H} > R_{O_1H}$ where we consider the proton to have transferred. This approach is similar to the one used to explore the extent of proton transfer in $F^- \cdot (H_2O)$ complexes.[101]

In the case of $H_5O_2^+$, as the proton is equidistant from the two oxygen atoms in the minimum energy geometry, the probability amplitude in the two regions is equal. On the other hand, for $H_7O_3^+$ and $H_9O_4^+$, there is significantly more amplitude in the region where $R_{O_2H} < R_{O_1H}$, and this effect is larger for $H_9O_4^+$ than for $H_7O_3^+$. The trends parallel the OH stretch frequencies mentioned above, thereby providing a qualitative, physical picture for how the trends seen in the spectroscopy relate to the structure of the system when nuclear quantum effects are included.

We can further explore how these trends are affected by deuteration by comparing the probability amplitudes obtained for the fully deuterated versions of the ions, shown in Figure 7D-F, to those shown in panels A-C. In the case of $H_5O_2^+$, on average the excess proton is equidistant between the two oxygen atoms, and deuteration does not affect this symmetry. On the other hand, the amplitude of the motion decreases with deuteration. This decrease in the amplitude of the vibrational motion with deuteration is also seen in the probability amplitudes for $H_7O_3^+$ and $H_9O_4^+$. The more compact wave function is reflected in decreases in the percentage of the probability amplitude in the motion that is able to access the region of configuration space where $R_{O_2H} > R_{O_1H}$ by a factor of 2 for $H_7O_3^+$, and a factor of nearly 2.5 for $H_9O_4^+$. These changes are consistent with expectations based on the generally smaller amplitude of an OD vibration compared to OH, although the magnitude of the effect is hard to anticipate. DMC studies make the exploration of such questions accessible for investigation.

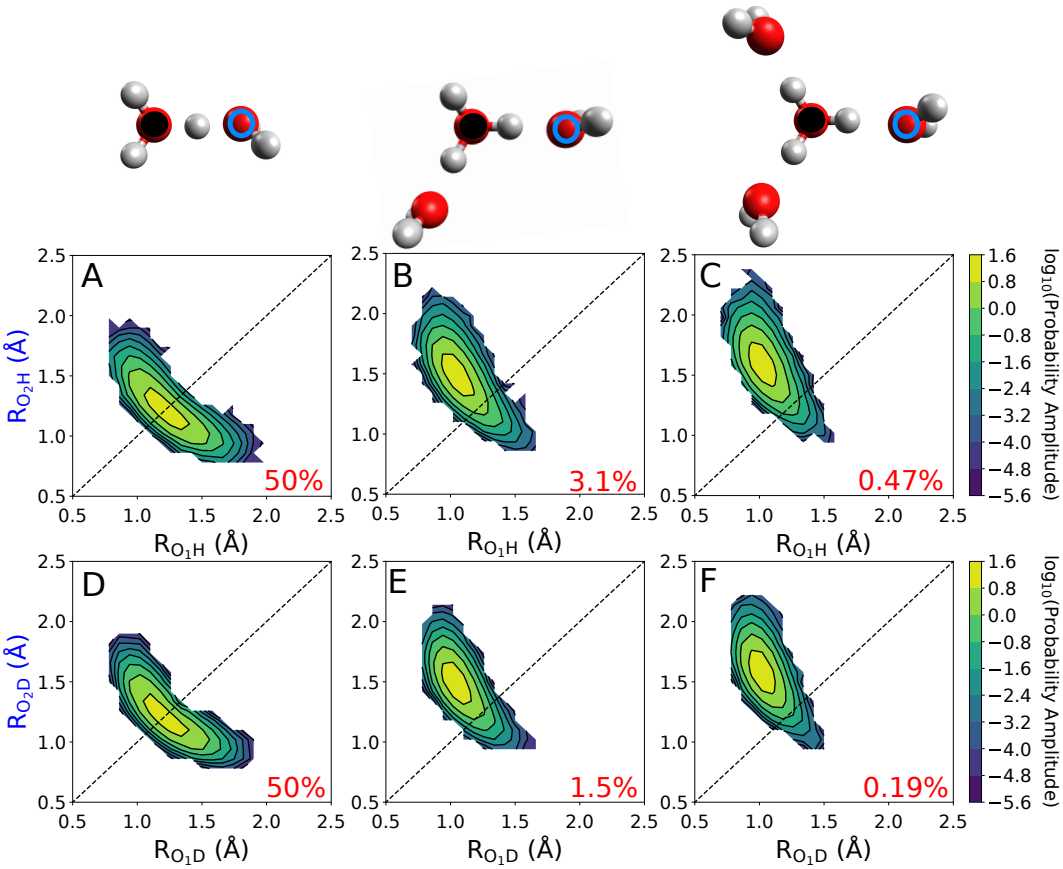

Figure 7: Projections of the probability amplitude onto $R_{\mathrm{O_1H}}$, the distance between the shared proton and the oxygen in the hydronium core (identified with the black filled circle in the structures) and $R_{\mathrm{O_2H}}$, the distance between the shared proton and the oxygen in the bonded water molecule (identified with the blue unfilled circle) for (A) $H_5O_2^+$, (B) $H_7O_3^+$, and (C) $H_9O_4^+$, and their corresponding deuterated analogs (D-F) . The dotted line indicates when $R_{\mathrm{O_1H}} = R_{\mathrm{O_2H}}$, which is the point at which the shared proton is equidistant from the two oxygen atoms. The number reported in red provides the percentage of the probability amplitude for which $R_{\mathrm{O_1H}} > R_{\mathrm{O_2H}}$. Details of the DMC simulations are provided in Appendix SA.

7 Conclusions, ongoing challenges and future directions

Diffusion Monte Carlo provides a powerful tool for understanding the vibrational landscape and spectroscopy of highly anharmonic molecular systems. One of the exciting aspects of DMC is the fact that while it utilizes many of the familiar tools of quantum mechanics, the stochastic nature of the approach provides opportunities to move beyond the usual strategy of developing a zero-order Hamiltonian and basis. This aspect of the method is what makes it particularly powerful for studying molecules and molecular ions that undergo large amplitude motions. In the above discussion, we focused on protonated water clusters. Similar strategies can be used to gain insights into other molecular and ionic clusters, molecules of astrochemical interest such as $H^+ \cdot (H_2)_n$, or protonated hydrocarbons, all of which undergo large amplitude vibrational motions even in their ground states.

The discussion in this contribution serves to illustrate that while DMC can be used to obtain physical insights into molecular structure and bonding, and how these properties manifest in the vibrational spectroscopy, complications remain that make it difficult to fully address the challenge laid out by Dirac in 1929.[1] The first issue is in the scaling and computational cost associated with DMC simulations.[48, 102] In principle, the cost of a simulation should scale with the cost of the potential calls. However, in practice the size of the ensemble required to obtain accurate results also grows with system size. The use of the guided DMC approach described above leads to a significant reduction in the ensemble size required to obtain a high-quality ground state wave function and zero-point energy, with only a small increase in the computational cost. While this strategy renders studies of systems with up to 20 atoms feasible, at some point these calculations will also become computationally intractable.

A second and perhaps larger challenge to extending the systems for which DMC calculations are performed is the availability of potential surfaces with sufficient accuracy to obtain meaningful results, and which can be evaluated efficiently. The highly accurate protonated water cluster surface used for this study was fit to tens of thousands of CCSD(T) calculations.[51, 50] While the evaluation of this potential is substantially less expensive than the underlying electronic structure calculations, it still uses approximately 95% of the time of the calculation.

One strategy for addressing these challenges is to utilize the recent advances in data science and machine learning, and develop a workflow in which the potential surface for the system of interest is fit using neural networks. The general strategy of this approach involves using small-scale DMC simulations to collect training data,[47] which is then developed into a fit surface using a multi-layered neural network. The benefit of this approach is that the neural network can be evaluated in a massively parallel fashion through the use of Graphics Processing Units (GPUs), making the evaluation of the neural network compared to the analogous CPU-based potentials faster by an order of magnitude or more. This strategy also opens the possibility to obtaining potential surfaces on-the-fly, further extending the reach of DMC calculations.

A third challenge remains in calculating states beyond the ground state. This has been and continues to be an active area of research in our group.

One final challenge with DMC is the lack of an available standard software package for performing DMC simulations. As mentioned previously, our group has introduced PyVibDMC, a general purpose Python package for performing DMC simulations for vibrational problems.[30] With PyVibDMC, we hope to standardize how DMC simulations are performed while also providing an efficient implementation that is easy to use by members of the community.

Acknowledgments

Support from the Chemistry Division of the National Science Foundation (CHE-1856125) is gratefully acknowledged. Parts of this work were performed using the Ilahie cluster, which was purchased using funds from a MRI grant from the National Science Foundation (CHE-1624430). This work was also facilitated through the use of advanced computational, storage, and networking infrastructure provided by the Hyak supercomputer system and funded by the STF at the University of Washington. This research also used resources of the National Energy Research Scientific Computing Center, a DOE Office of Science User Facility supported by the Office of Science of the U.S. Department of Energy under Contract No. DE-AC02-05CH11231 using NERSC award BES-ERCAP0020502. The development of PyVibDMC was supported by a fellowship from The Molecular Sciences Software Institute to RJD under NSF grant OAC-1547580.

Conflict of interest

The authors have declared no conflicts of interest for this article.

Data availability statement

The data that supports the findings of this study are available in the supplementary material of this article

References

[1] Dirac PAM, Fowler RH. Quantum Mechanics of Many-Electron Systems. Proceedings of the Royal Society of London Series A, Containing Papers of a Mathematical and Physical Character. 1929;123(792):714–733. Available from: https://royalsocietypublishing.org/doi/abs/10.1098/rspa.1929.0094.

[2] Scemama A, Caffarel M, Oseret E, Jalby W. QMC=Chem: A Quantum Monte Carlo Program for Large-Scale Simulations in Chemistry at the Petascale Level and Beyond. In: Daydé M, Marques O, Nakajima K, editors. High Performance Computing for Computational Science - VECPAR 2012. Berlin, Heidelberg: Springer Berlin Heidelberg; 2013. p. 118–127.

[3] Kent PRC, Annaberdiyev A, Benali A, Bennett MC, Landinez Borda EJ, Doak P, et al. QMCPACK: Advances in the Development, Efficiency, and Application of Auxiliary Field and Real-Space Variational and Diffusion Quantum Monte Carlo. J Chem Phys. 2020;152(17):174105. Available from: https://doi.org/10.1063/5.0004860.

[4] Lüchow A. Quantum Monte Carlo Methods. WIREs Comput Mol Sci. 2011;1:388–402.

[5] Zhang S, Motta M. Ab Initio Computations of Molecular Systems by the Auxiliary-Field Quantum Monte Carlo Method. WIREs Comput Mol Sci. 2018;8:1–29.

[6] Pineda Flores SD, Neuscamman E. Excited State Specific Multi-Slater Jastrow Wave Functions. J Phys Chem A. 2019;123(8):1487–1497. PMID: 30702890. Available from: https://doi.org/10.1021/acs.jpca.8b10671.

[7] Lester WA, editor. Recent Advances in Quantum Monte Carlo Methods. Recent Advances in Computational Chemistry - Vol. 2. Singapore: World Scientific; 1997.

[8] Lester WA, Rothstein SM, Tanaka S, editors. Recent Advances in Quantum Monte Carlo Methods, Part II. Recent Advances in Computational Chemistry - Vol. 2. Singapore: World Scientific; 2002.

[9] Anderson JB, Rothstein SM, editors. Advances in Quantum Monte Carlo Methods. vol. 953 of ACS Symposium Series. Washington, DC: American Chemical Society; 2007.

[10] Tanaka S, Rothstein SM, Lester WA, editors. Advances in Quantum Monte Carlo Methods. vol. 1094 of ACS Symposium Series. Washington, DC: American Chemical Society; 2012.

[11] Tanaka S, Roy PN, Mitas L, editors. Recent Progress in Quantum Monte Carlo Methods. vol. 1234 of ACS Symposium Series. Washington, DC: American Chemical Society; 2016.

[12] Barone V. Anharmonic Vibrational Properties by a Fully Automated Second-Order Perturbative Approach. J Chem Phys. 2005;122(1):014108. Available from: https://doi.org/10.1063/1.1824881.

[13] Franke PR, Stanton JF, Douberly GE. How to VPT2: Accurate and Intuitive Simulations of CH Stretching Infrared Spectra Using VPT2+K with Large Effective Hamiltonian Resonance Treatments. J Phys Chem A. 2021;125(6):1301–1324. Available from: https://doi.org/10.1021/acs.jpca.0c09526.

[14] Gozem S, Krylov AI. The ezSpectra Suite: An Easy-to-use Toolkit for Spectroscopy Modeling. WIREs Comput Mol Sci. 2021;p. 1–22.

[15] Carrington T, Wang X. Computing Ro-Vibrational Spectra of van der Waals Molecules. WIREs Comput Mol Sci. 2011 doi: 101002/wcms73;1:952–963.

[16] Meyer H. Studying Molecular Quantum Dynamics with the Multiconfiguration Time-Dependent Hartree Method. WIREs Comput Mol Sci. 2012;2:351–374.

[17] DiRisio RJ, McCoy AB. rjdirisio/pyvibdmc:1.1.8. Zenodo; 2021. Available from: https://doi.org/10.5281/zenodo.4695231.

[18] Hammer NI, Diken EG, Roscioli JR, Johnson MA, Myshakin EM, Jordan KD, et al. The Vibrational Predissociation Spectra of the $H_5O_2^+ \cdot RG_n$(RG=Ar,Ne) Clusters: Correlation of the Solvent Perturbations in the Free OH and Shared Proton Transitions of the Zundel Ion. J Chem Phys. 2005;122(24):244301. Available from: https://doi.org/10.1063/1.1927522.

[19] Asmis KR, Pivonka NL, Santambrogio G, Bruemmer M, Kaposta C, Neumark DM, et al. Gas-Phase Infrared Spectrum of the Protonated Water Dimer. Science. 2003;299:1375–77.

[20] Headrick JM, Diken EG, Walters RS, Hammer NI, Christie RA, Cui J, et al. Spectral Signatures of Hydrated Proton Vibrations in Water Clusters. Science. 2005;308(5729):1765–1769. Available from: http://science.sciencemag.org/content/308/5729/1765.

[21] Douberly GE, Walters RS, Cui J, Jordan KD, Duncan MA. Infrared Spectroscopy of Small Protonated Water Clusters, $H^+(H_2O)_n$ ($n = 2-5$): Isomers, Argon Tagging, and Deuteration. J Phys Chem A. 2010;114(13):4570–4579. Available from: https://doi.org/10.1021/jp100778s.

[22] Heine N, Fagiani MR, Rossi M, Wende T, Berden G, Blum V, et al. Isomer-Selective Detection of Hydrogen-Bond Vibrations in the Protonated Water Hexamer. J Am Chem Soc. 2013;135(22):8266–8273.

[23] Heine N, Fagiani MR, Asmis KR. Disentangling the Contribution of Multiple Isomers to the Infrared Spectrum of the Protonated Water Heptamer. J Phys Chem Lett. 2015;6(12):2298–2304. PMID: 26266608. Available from: https://doi.org/10.1021/acs.jpclett.5b00879.

[24] Fagiani MR, Knorke H, Esser TK, Heine N, Wolke CT, Gewinner S, et al. Gas Phase Vibrational Spectroscopy of the Protonated Water Pentamer: The Role of Isomers and Nuclear Quantum Effects. Phys Chem Chem Phys. 2016;18:26743–26754. Available from: http://dx.doi.org/10.1039/C6CP05217G.

[25] Esser TK, Knorke H, Asmis KR, Schöllkopf W, Yu Q, Qu C, et al. Deconstructing Prominent Bands in the Terahertz Spectra of $H_7O_3^+$ and $H_9O_4^+$: Intermolecular Modes in Eigen Clusters. J Phys Chem Lett. 2018;9(4):798–803. Available from: https://doi.org/10.1021/acs.jpclett.7b03395.

[26] Wolke CT, Fournier JA, Dzugan LC, Fagiani MR, Odbadrakh TT, Knorke H, et al. Spectroscopic Snapshots of the Proton-Transfer Mechanism in Water. Science. 2016;354(6316):1131–1135. Available from: http://science.sciencemag.org/content/354/6316/1131.

[27] Duong CH, Yang N, Kelleher PJ, Johnson MA, DiRisio RJ, McCoy AB, et al. Tag-Free and Isotopomer-Selective Vibrational Spectroscopy of the Cryogenically Cooled $H_9O_4^+$ Cation

with Two-Color, IR–IR Double-Resonance Photoexcitation: Isolating the Spectral Signature of a Single OH Group in the Hydronium Ion Core. J Phys Chem A. 2018;122(48):9275–9284. Available from: https://doi.org/10.1021/acs.jpca.8b08507.

[28] Duong CH, Gorlova O, Yang N, Kelleher PJ, Johnson MA, McCoy AB, et al. Disentangling the Complex Vibrational Spectrum of the Protonated Water Trimer, $H^+(H_2O)_3$, with Two-Color IR-IR Photodissociation of the Bare Ion and Anharmonic VSCF/VCI Theory. J Phys Chem Lett. 2017;8(16):3782–3789. Available from: https://doi.org/10.1021/acs.jpclett.7b01599.

[29] Duong CH, Yang N, Johnson MA, DiRisio RJ, McCoy AB, Yu Q, et al. Disentangling the Complex Vibrational Mechanics of the Protonated Water Trimer by Rational Control of Its Hydrogen Bonds. J Phys Chem A. 2019;123(37):7965–7972. Available from: https://doi.org/10.1021/acs.jpca.9b05576.

[30] DiRisio RJ, Lu F, McCoy AB. rjdirisio/pyvibdmc:1.3.4. Zenodo; 2021. Available from: https://doi.org/10.5281/zenodo.5787036.

[31] Metropolis N, Ulam S. The Monte Carlo Method. J Am Stat Assoc. 1949;44:334–341.

[32] Anderson JB. A Random-Walk Simulation of the Schrödinger Equation: H_3^+. J Chem Phys. 1975;63(4):1499–1503. Available from: https://doi.org/10.1063/1.431514.

[33] McCoy AB. Diffusion Quantum Monte Carlo on Multiple Potential Surfaces. Chem Phys Lett. 2000;321:71–77.

[34] McCoy AB. Diffusion Monte Carlo Approaches for Investigating the Structure and Vibrational Spectra of Fluxional Systems. Int Rev Phys Chem. 2006;25(1-2):77–107. Available from: https://doi.org/10.1080/01442350600679347.

[35] Trotter HF. On the Product of Semi-Groups of Operators. Proc Amer Math Soc. 1959;10:545–551.

[36] Suzuki M. Generalized Trotter's Formula and Systematic Approximants of Exponential Operators and Inner Derivations with applications to many-body problems. Comm Math Phys. 1976;51(2):183–190. Available from: https://doi.org/10.1007/BF01609348.

[37] Feit MD, Fleck JA. Solution of the Schrödinger Equation by a Spectral Method II: Vibrational Energy Levels of Triatomic molecules. J Chem Phys. 1983;p. 301–8.

[38] Reynolds PJ, Ceperley DM, Alder BJ, Lester WA. Fixed-Node Quantum Monte Carlo for Molecules. J Chem Phys. 1982;77(11):5593–5603. Available from: https://doi.org/10.1063/1.443766.

[39] Suhm MA, Watts RO. Quantum Monte Carlo Studies of Vibrational States in Molecules and Clusters. Phys Rep. 1991;204(4):293 – 329. Available from: http://www.sciencedirect.com/science/article/pii/037015739190136A.

[40] Finney JM, DiRisio RJ, McCoy AB. Guided Diffusion Monte Carlo: A Method for Studying Molecules and Ions that Display Large Amplitude Vibrational Motions. J Phys Chem A. 2020;124(46):9567–9577.

[41] Anderson JB. Quantum Chemistry by Random Walk. H ^2P, H_3^+ D_{3h} $^1A_1'$, H_2 $^3\Sigma_u^+$, H_4 $^1\Sigma_g^+$, Be ^1S. J Chem Phys. 1976;65(10):4121–4127. Available from: https://doi.org/10.1063/1.432868.

[42] Petit AS, Wellen BA, McCoy AB. Using Fixed-Node Diffusion Monte Carlo to Investigate the Effects of Rotation-Vibration Coupling in Highly Fluxional Asymmetric Top Molecules: Application to H_2D^+. J Chem Phys. 2013;138(3):034105. Available from: https://doi.org/10.1063/1.4774318.

[43] Barone V, Alessandrini S, Biczysko M, Cheeseman JR, Clary DC, McCoy AB, et al. Computational Molecular Spectroscopy. Nature Reviews Methods Primers. 2021;1(1):38. Available from: https://doi.org/10.1038/s43586-021-00034-1.

[44] Petit AS, McCoy AB. Diffusion Monte Carlo in Internal Coordinates. J Phys Chem A. 2013;117(32):7009–7018. Available from: https://doi.org/10.1021/jp312710u.

[45] Buch V. Treatment of Rigid Bodies by Diffusion Monte Carlo: Application to the para-$H_2 \cdots H_2O$ and ortho-$H_2 \cdots H_2O$ Clusters. J Chem Phys. 1992;97(1):726–729. Available from: https://doi.org/10.1063/1.463572.

[46] Benoit DM, Clary DC. Quaternion Formulation of Diffusion Quantum Monte Carlo for the Rotation of Rigid Molecules in Clusters. J Chem Phys. 2000;113:5193–5202.

[47] DiRisio RJ, Lu F, McCoy AB. GPU-accelerated Neural Network Potential Energy Surfaces for Diffusion Monte Carlo. J Phys Chem A. 2021;125(26):5849–5859. Available from: https://doi.org/10.1021/acs.jpca.1c03709.

[48] Lee VGM, Vetterli NJ, Boyer MA, McCoy AB. Diffusion Monte Carlo Studies on the Detection of Structural Changes in the Water Hexamer upon Isotopic Substitution. J Phys Chem A. 2020 08;124(34):6903–6912. Available from: https://doi.org/10.1021/acs.jpca.0c05686.

[49] Qu C, Yu Q, Bowman JM. Permutationally Invariant Potential Energy Surfaces. Annual Review of Physical Chemistry. 2018;69(1):151–175. PMID: 29401038. Available from: https://doi.org/10.1146/annurev-physchem-050317-021139.

[50] Huang X, Braams BJ, Bowman JM. *Ab initio* Potential Energy and Dipole Moment Surfaces for $H_5O_2^+$. J Chem Phys. 2005;122:044308.

[51] Yu Q, Bowman JM. Communication: VSCF/VCI Vibrational Spectroscopy of $H_7O_3^+$ and $H_9O_4^+$ Using High-Level, Many-Body Potential Energy Surface and Dipole Moment Surfaces. J Chem Phys. 2017;146(12):121102. Available from: https://doi.org/10.1063/1.4979601.

[52] Jin Z, Braams BJ, Bowman JM. An ab Initio Based Global Potential Energy Surface Describing $CH_5^+ \rightarrow CH_3^+ + H_2$. J Phys Chem A. 2006;110:1569–1574.

[53] Acioli PH, Xie Z, Braams BJ, Bowman JM. Vibrational Ground State Properties of H_5^+ and its Isotopomers from Diffusion Monte Carlo Calculations. J Chem Phys. 2008;128:104318.

[54] Wang Y, Shepler BC, Braams BJ, Bowman JM. Full-Dimensional, ab Initio Potential Energy and Dipole Moment Surfaces for Water. The Journal of Chemical Physics. 2009;131(5):054511. Available from: https://aip.scitation.org/doi/abs/10.1063/1.3196178.

[55] Wang Y, Huang X, Shepler BC, Braams BJ, Bowman JM. Flexible, ab Initio Potential, and Dipole Moment Surfaces for Water. I. Tests and Applications for Clusters up to the

22-mer. The Journal of Chemical Physics. 2011;134(9):094509. Available from: https://doi.org/10.1063/1.3554905.

[56] Wang Y, Bowman JM. Ab initio Potential and Dipole Moment Surfaces for Water. II. Local-Monomer calculations of the Infrared Spectra of Water Clusters. J Chem Phys. 2011;134(15):154510. Available from: https://doi.org/10.1063/1.3579995.

[57] Paesani F. Getting the Right Answers for the Right Reasons: Toward Predictive Molecular Simulations of Water with Many-Body Potential Energy Functions. Acc Chem Res. 2016;49(9):1844–1851. Available from: https://doi.org/10.1021/acs.accounts.6b00285.

[58] Babin V, Leforestier C, Paesani F. Development of a "First Principles" Water Potential with Flexible Monomers: Dimer Potential Energy Surface, VRT Spectrum, and Second Virial Coefficient. J Chem Theory Comput. 2013;9(12):5395–5403. PMID: 26592277. Available from: https://doi.org/10.1021/ct400863t.

[59] Babin V, Medders GR, Paesani F. Development of a "First Principles" Water Potential with Flexible Monomers. II: Trimer Potential Energy Surface, Third Virial Coefficient, and Small Clusters. J Chem Theory Comput. 2014;10(4):1599–1607. Available from: https://doi.org/10.1021/ct500079y.

[60] Medders GR, Babin V, Paesani F. Development of a "First-Principles" Water Potential with Flexible Monomers. III. Liquid Phase Properties. J Chem Theory Comput. 2014;10(8):2906–2910. PMID: 26588266. Available from: https://doi.org/10.1021/ct5004115.

[61] Colbert DT, Miller WH. A Novel Discrete Variable Representation for Quantum Mechanical Reactive Scattering via the S-matrix Kohn Method. J Chem Phys. 1992;96:1982–1991.

[62] Bulik IW, Frisch MJ, Vaccaro PH. Fixed-Node, Importance-Sampling Diffusion Monte Carlo for Vibrational Structure with Accurate and Compact Trial States. J Chem Theory Comput. 2018;14(3):1554–1563. Available from: https://doi.org/10.1021/acs.jctc.8b00016.

[63] Lee VGM, Madison LR, McCoy AB. Evaluation of Matrix Elements Using Diffusion Monte Carlo Wave Functions. J Phys Chem A. 2019 05;123(20):4370–4378. Available from: https://doi.org/10.1021/acs.jpca.8b11213.

[64] Jastrow R. Many-Body Problem with Strong Forces. Phys Rev. 1955 Jun;98:1479–1484. Available from: https://link.aps.org/doi/10.1103/PhysRev.98.1479.

[65] Bacic Z, Kennedy-Mandziuk M, Moskowitz JW, Schmidt KE. He_2Cl_2 and He_3Cl_2 van der Waals Clusters: A Quantum Monte Carlo Study. J Chem Phys. 1992;97(9):6472–6480. Available from: https://doi.org/10.1063/1.463708.

[66] Niyaz P, Bacic Z, Moskowitz JW, Schmidt KE. Ar_nHF ($n = 1-4$) van der Waals Clusters: A Quantum Monte Carlo Study of Ground State Energies, Structures and HF Vibrational Frequency Shifts. Chem Phys Lett. 1996;252(1):23–32. Available from: https://www.sciencedirect.com/science/article/pii/S0009261496001248.

[67] Sarsa A, Bacic Z, Moskowitz JW, Schmidt KE. HF Dimer in Small Helium Clusters: Interchange-Tunneling Dynamics in a Quantum Environment. Phys Rev Lett. 2002;88:123401/1–123401/4.

[68] Huang X, Cho HM, Carter S, Ojamäe L, Bowman JM, Singer SJ. Full Dimensional Quantum Calculations of Vibrational Energies of $H_5O_2^+$. J Phys Chem A. 2003;107(37):7142–7151. Available from: https://doi.org/10.1021/jp035081a.

[69] da Silva WB, Acioli PH. Trial Wave Functions for the Calculation of Vibrational States of Molecules Using Quantum Monte Carlo. J Chem Phys. 2001;114(22):9720–9724. Available from: https://doi.org/10.1063/1.1370533.

[70] Guardiola R, Navarro J. A Diffusion Monte Carlo Study of Small Para-Hydrogen Clusters. Open Phys. 2008 Mar;6(1):33–37. Available from: https://doi.org/10.2478/s11534-008-0019-z.

[71] Sola E, Boronat J. Solidification of Small p-H2 Clusters at Zero Temperature. J Phys Chem A. 2011;115(25):7071–7076. Available from: https://doi.org/10.1021/jp112378h.

[72] Kohno BH, Mandelshtam VA. The Loss of Size Sensitivity in para-Hydrogen Clusters Due to the Strong Quantum Delocalization. J Phys Chem A. 2020;124(42):8766–8777. Available from: https://doi.org/10.1021/acs.jpca.0c07107.

[73] Mallory JD, Mandelshtam VA. Quantum Melting and Isotope Effects from Diffusion Monte Carlo Studies of p-H2 Clusters. J Phys Chem A. 2017;121(33):6341–6348. Available from: https://doi.org/10.1021/acs.jpca.7b06649.

[74] Lee VGM, McCoy AB. An Efficient Approach for Studies of Water Clusters Using Diffusion Monte Carlo. J Phys Chem A. 2019;123(37):8063–8070. Available from: https://doi.org/10.1021/acs.jpca.9b06444.

[75] Lin Z, McCoy AB. Investigation of the Structure and Spectroscopy of H_5^+ Using Diffusion Monte Carlo. J Phys Chem A. 2013;117(46):11725–11736. Available from: https://doi.org/10.1021/jp4014652.

[76] McCoy AB, Braams BJ, Brown A, Huang X, Jin Z, Bowman JM. Ab Initio Diffusion Monte Carlo Calculations of the Quantum Behavior of CH_5^+ in Full Dimensionality. J Phys Chem A. 2004;108(23):4991–4994. Available from: https://doi.org/10.1021/jp0487096.

[77] Fore ME, McCoy AB. Statistical Analysis of the Effect of Deuteration on Quantum Delocalization in CH_5^+. J Phys Chem A. 2019 05;123(21):4623–4631. Available from: https://doi.org/10.1021/acs.jpca.9b02685.

[78] McCunn LR, Roscioli JR, Johnson MA, McCoy AB. An H/D Isotopic Substitution Study of the $H_5O_2^+$·Ar Vibrational Predissociation Spectra: Exploring the Putative Role of Fermi Resonances in the Bridging Proton Fundamentals. J Phys Chem B. 2008;112(2):321–327. Available from: https://doi.org/10.1021/jp075289m.

[79] DiRisio RJ, Finney JM, Dzugan LC, Madison LR, McCoy AB. Using Diffusion Monte Carlo Wave Functions to Analyze the Vibrational Spectra of $H_7O_3^+$ and $H_9O_4^+$. J Phys Chem A. 2021;125(33):7185–7197. Available from: https://doi.org/10.1021/acs.jpca.1c05025.

[80] Barnett RN, Reynolds PJ, W A Lester J. Monte Carlo Algorithms for Expectation Values of Coordinate Operators. J Comput Phys. 1991;96(2):258 – 276. Available from: http://www.sciencedirect.com/science/article/pii/002199919190236E.

[81] Sandler P, Buch V, Clary DC. Calculation of Expectation Values of Molecular Systems Using Diffusion Monte Carlo in Conjunction With the Finite Field Method. J Chem Phys. 1994;101:6353–5.

[82] Lee HS, Herbert JM, McCoy AB. Adiabatic Diffusion Monte Carlo Approaches for Studies of Ground and Excited State Properties of van der Waals Complexes. J Chem Phys. 1999;110(12):5481–5484. Available from: https://doi.org/10.1063/1.478444.

[83] Lee HS, McCoy AB. Quantum Monte Carlo Studies of the Structure and Spectroscopy of the Ne_nOH ($\tilde{A}\,^2\Sigma^+, n = 1-4$) van der Waals Complexes. J Chem Phys. 2001;114:10278–87.

[84] Lee HS, Herbert JM, McCoy AB. Structure and Spectroscopy of Ne_nSH ($\tilde{A}^2\Sigma^+$) Complexes Using Adiabatic Diffusion Monte Carlo (ADMC). J Chem Phys. 1999;111(20):9203–9212. Available from: https://doi.org/10.1063/1.479834.

[85] McCoy AB. Diffusion Monte Carlo Approaches for Studying Systems that Undergo Large Amplitude Vibrational Motions. In: Anderson JB, Rothstein SM, editors. Recent Advances in Quantum Monte Carlo Methods. vol. 3. ACS Symposium Series 953; 2006. p. 147–164.

[86] Barnett RN, Reynolds PJ, Lester WA. Computation of Transition Dipole Moments by Monte Carlo. J Chem Phys. 1992;96(3):2141–2154. Available from: https://doi.org/10.1063/1.462065.

[87] Finney JM, DiRisio RJ, McCoy AB. Diffusion Monte Carlo Approaches for Studying Large Amplitude Vibrational Motions in Molecules and Clusters; 2022. submitted as a chapter in *A Computational Approach to Vibrational Dynamics of Molecules*, edited by J. M. Bowman.

[88] Lee HS, McCoy AB. Variational Calculations of Weakly Bound Trimers: Studies of the Spectra of Ne_2·OH and SH ($\tilde{A}\,^2\Sigma^+$). J Chem Phys. 2002;116:9677–9689.

[89] McCoy AB, Huang X, Carter S, Bowman JM. Quantum Studies of the Vibrations in $H_3O_2^-$ and $D_3O_2^-$. J Chem Phys. 2005;123(6):064317. Available from: https://doi.org/10.1063/1.2001654.

[90] Lin Z, McCoy AB. Signatures of Large-Amplitude Vibrations in the Spectra of H_5^+ and D_5^+. J Phys Chem Lett. 2012;3(24):3690–3696. Available from: https://doi.org/10.1021/jz3017683.

[91] Wilson EB, Decius JC, Cross PC. Molecular Vibrations. New York: Dover; 1955.

[92] Sandler P, Buch V, Sadlej J. Ground and Excited States of the Complex of CO With Water: A Diffusion Monte Carlo Study. J Chem Phys. 1996;105:10387–10397.

[93] Severson MW, Buch V. Quantum Monte Carlo Simulation of Intermolecular Excited Vibrational States in the Cage Water Hexamer. J Chem Phys. 1999;111:10866–10875.

[94] McCoy AB, Diken EG, Johnson MA. Generating Spectra from Ground-State Wave Functions: Unraveling Anharmonic Effects in the OH^-·H_2O Vibrational Predissociation Spectrum. J Phys Chem A. 2009;113(26):7346–7352. Available from: https://doi.org/10.1021/jp811352c.

[95] Guasco TL, Johnson MA, McCoy AB. Unraveling Anharmonic Effects in the Vibrational Predissociation Spectra of $H_5O_2^+$ and Its Deuterated Analogues. J Phys Chem A. 2011;115(23):5847–5858. Available from: https://doi.org/10.1021/jp109999b.

[96] Bowman JM, Carter S, Huang X. MULTIMODE: a Code to Calculate Rovibrational Energies of Polyatomic Molecules. Int Rev Phys Chem. 2003;22:533–549.

[97] Stringer AD, Curotto E. An Ergodic Measure for Diffusion Monte Carlo Ground State Wavefunctions: Application to a Hydrogen Cluster With an Isotopic Impurity. Chemical Physics Letters. 2019;734:136728. Available from: https://www.sciencedirect.com/science/article/pii/S0009261419307092.

[98] Vendrell O, Gatti F, Meyer HD. Full Dimensional (15-dimensional) Quantum-Dynamical Simulation of the Protonated Water Dimer. II. Infrared Spectrum and Vibrational Dynamics. J Chem Phys. 2007;127:184303.

[99] Yu Q, Bowman JM. High-Level Quantum Calculations of the IR Spectra of the Eigen, Zundel, and Ring Isomers of $H^+(H_2O)_4$ Find a Single Match to Experiment. J Am Chem Soc. 2017;139(32):10984–10987. Available from: https://doi.org/10.1021/jacs.7b05459.

[100] McCoy AB, Dzugan LC, DiRisio RJ, Madison LR. Spectral Signatures of Proton Delocalization in $H^+(H_2O)_{n=1-4}$ Ions. Faraday Discuss. 2018;212:443–466. Available from: http://dx.doi.org/10.1039/C8FD00120K.

[101] Horvath S, McCoy AB, Roscioli JR, Johnson MA. Vibrationally Induced Proton Transfer in $F^-(H_2O)$ and $F^-(D_2O)$. J Phys Chem A. 2008;112(48):12337–12344. Available from: https://doi.org/10.1021/jp805616m.

[102] Mallory JD, Mandelshtam VA. Diffusion Monte Carlo Studies of MB-pol $(H_2O)_{2-6}$ and $(D_2O)_{2-6}$ Clusters: Structures and Binding Energies. J Chem Phys. 2016;145(6):064308. Available from: https://doi.org/10.1063/1.4960610.